

Highly selective hydrogenation of CO₂ to propane over GaZrO_x/H-SSZ-13 composite

In the format provided by the authors and unedited

Supplementary Information

Table of Contents

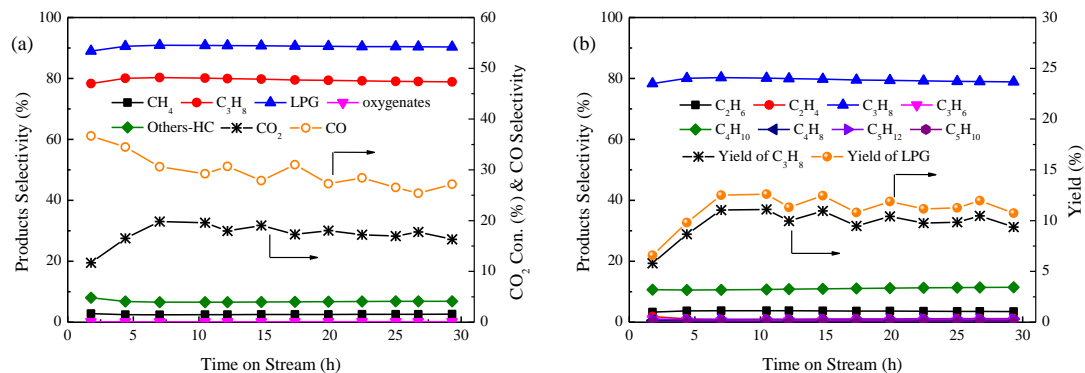
Supplementary Figures

Supplementary Tables

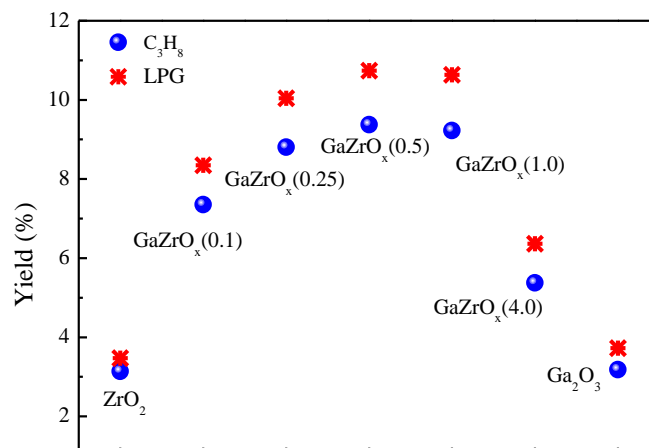
Supplementary Methods

Supplementary References

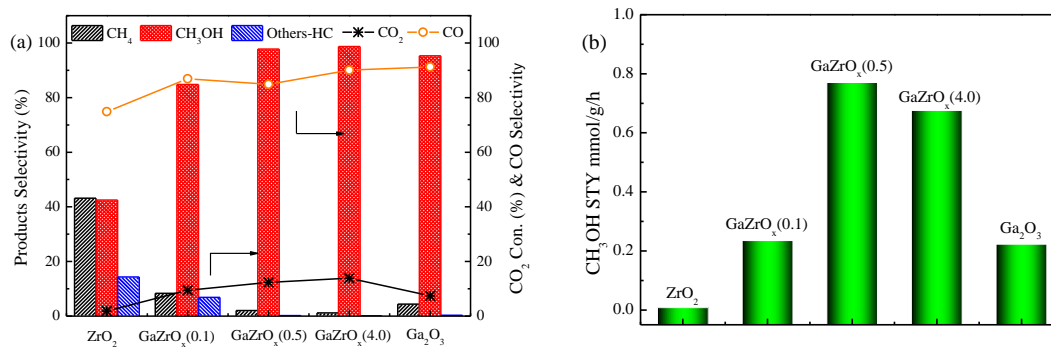
Supplementary Figures



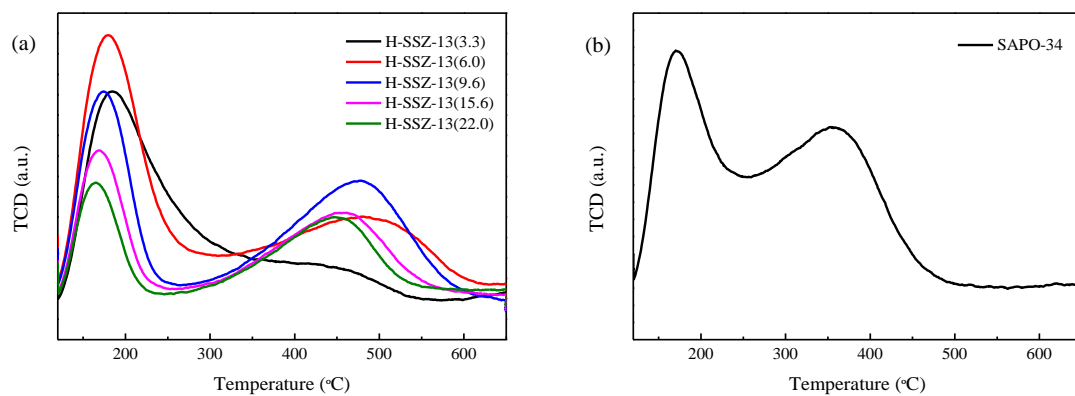
Supplementary Fig. 1. Catalytic performance for CO₂ hydrogenation. Evolutions of CO₂ conversion (a) and product selectivity (b) with reaction time over GaZrO_x(0.5)/H-SSZ-13(6.0) (typical reaction conditions: H₂/CO₂ = 3:1, GHSV = 2400 mL/(g·h), 3.0 MPa and 350 °C). Others-HC represents the selectivity of hydrocarbons, excluding the methane, propane and butane.



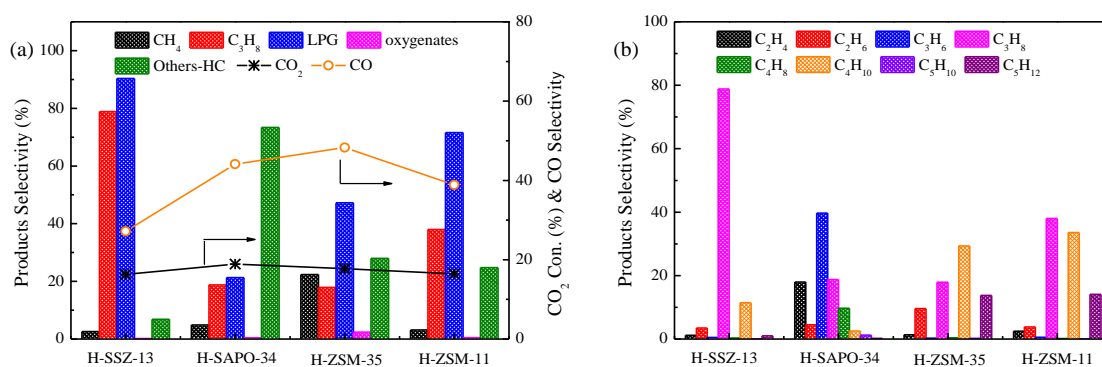
Supplementary Fig. 2. Propane and LPG yield. The yields of propane (C₃H₈) and LPG (propane+butane) for direct hydrogenation of CO₂ into propane over various composite catalysts consisting of H-SSZ-13(6.0) zeolite and GaZrO_x(N) oxide with different Ga/Zr molar ratios (typical reaction conditions: H₂/CO₂ = 3:1, GHSV = 2400 mL/(g·h), 3.0 MPa and 350 °C).



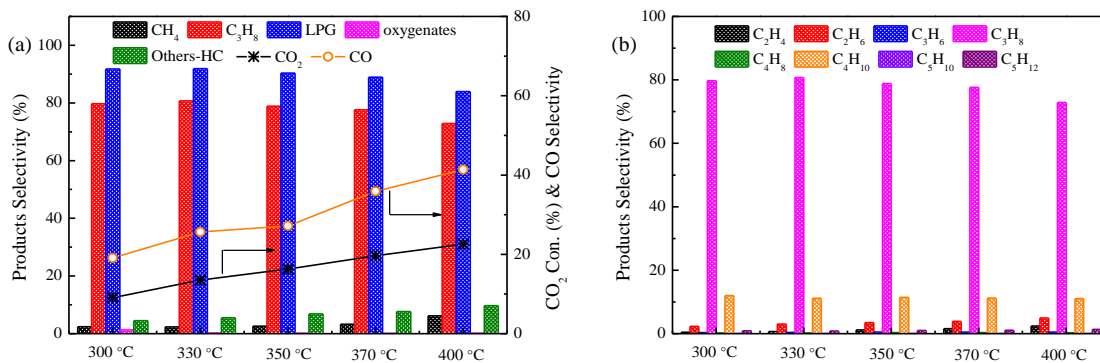
Supplementary Fig. 3. Catalytic performance for CO₂ hydrogenation. CO₂ conversion and product selectivity (a), and methanol space time yield (STY) (b) in CO₂ hydrogenation over various GaZrO_x(N) oxides (typical reaction conditions: H₂/CO₂ = 3:1, GHSV = 8000 mL/(g·h), 3.0 MPa and 350 °C). Others-HC represents the selectivity of hydrocarbons (alkenes + alkanes), excluding the methane. The CH₃OH is sum of methanol and dimethyl ether.



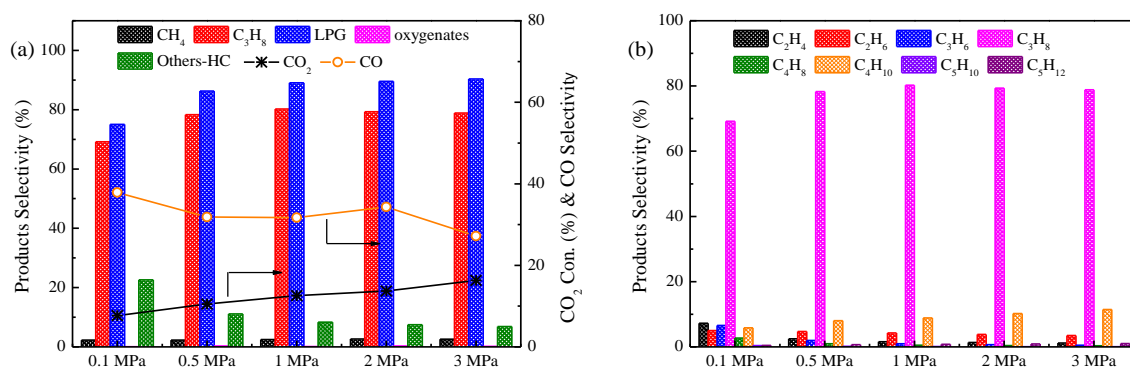
Supplementary Fig. 4. Acidic properties of zeolites. NH₃-TPD profiles of the H-SSZ-13 zeolites with different Si/Al ratios (a) and H-SAPO-34 zeolite (b).



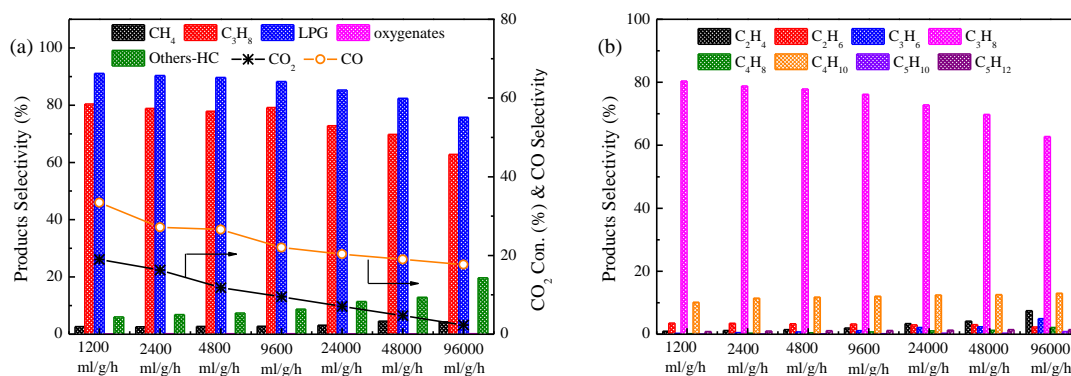
Supplementary Fig. 5. Catalytic performance for CO₂ hydrogenation. Catalytic results for direct hydrogenation of CO₂ into propane over composite catalyst system consisting of GaZrO_x(0.5) oxide and various zeolites (typical reaction conditions: H₂/CO₂ = 3:1, GHSV = 2400 mL/(g·h), 3.0 MPa and 350 °C). Others-HC represents the selectivity of hydrocarbons, excluding the methane, propane and butane.



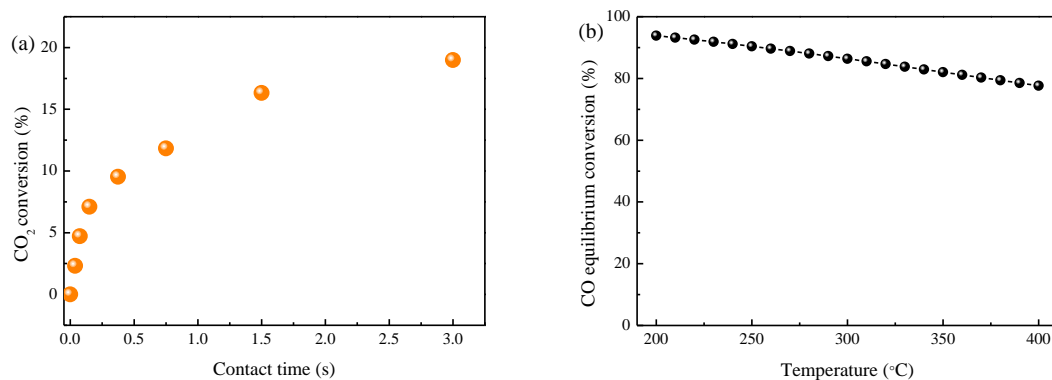
Supplementary Fig. 6. Catalytic performance for CO₂ hydrogenation. Influence of reaction temperature on CO₂ conversion and product selectivity in direct hydrogenation of CO₂ into propane over GaZrO_x(0.5)/H-SSZ-13(6.0) (typical reaction conditions: H₂/CO₂ = 3:1, GHSV = 2400 mL/(g·h) and 3.0 MPa). Others-HC represents the selectivity of hydrocarbons, excluding the methane, propane and butane.



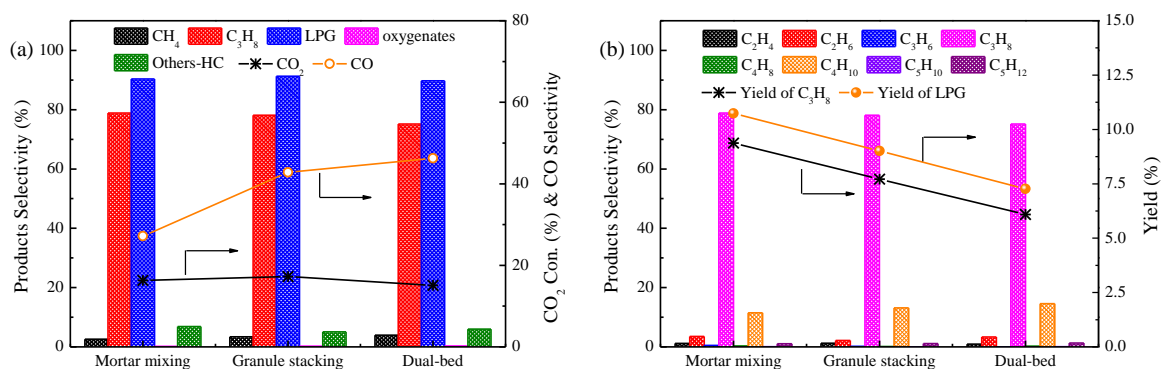
Supplementary Fig. 7. Catalytic performance for CO₂ hydrogenation. Effect of reaction pressure on CO₂ conversion and product selectivity on GaZrO_x(0.5)/H-SSZ-13(6.0) in direct hydrogenation of CO₂ into propane (typical reaction conditions: H₂/CO₂ = 3:1, GHSV = 2400 mL/(g·h) and 350 °C). Others-HC represents the selectivity of hydrocarbons, excluding the methane, propane and butane.



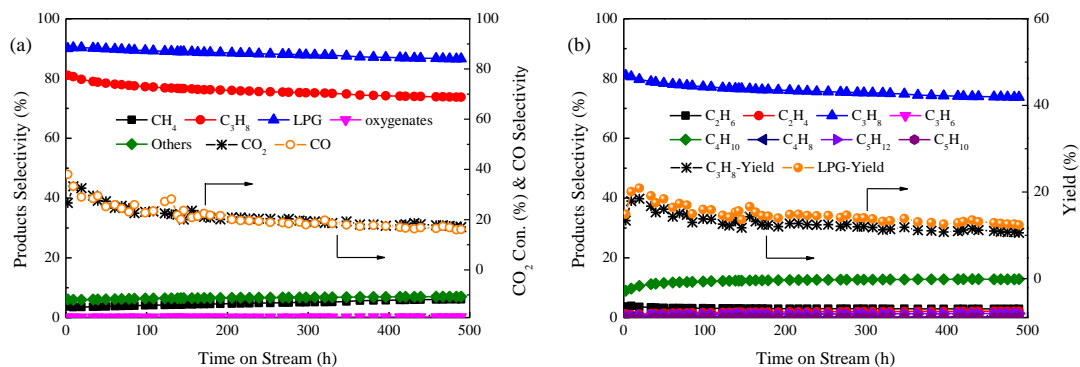
Supplementary Fig. 8. Catalytic performance for CO₂ hydrogenation. Influence of space velocity on CO₂ conversion and product selectivity obtained on GaZrO_x(0.5)/H-SSZ-13(6.0) in direct hydrogenation of CO₂ into propane (typical reaction conditions: H₂/CO₂ = 3:1, 3.0 MPa and 350 °C). Others-HC represents the selectivity of hydrocarbons excluding methane, propane and butane.



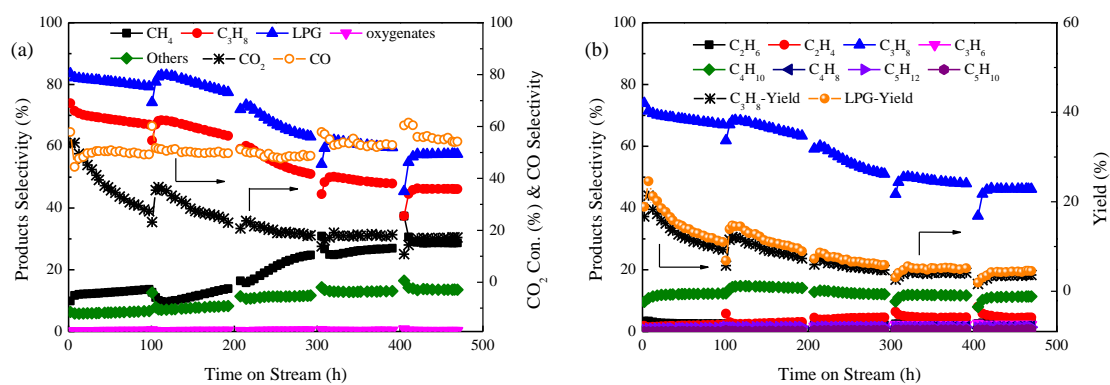
Supplementary Fig. 9. Kinetic and thermodynamic analysis. (a) Dependence of CO₂ conversion on contact time obtained on GaZrO_x(0.5)/H-SSZ-13(6.0) in CO₂ hydrogenation to propane (typical reaction conditions: H₂/CO₂ = 3:1, 3.0 MPa and 350 °C), and (b) CO equilibrium conversion for water-gas shift (WGS) reaction in the range of 200–400 °C at 3.0 MPa (The data was calculated by HSC chemistry 6.0).



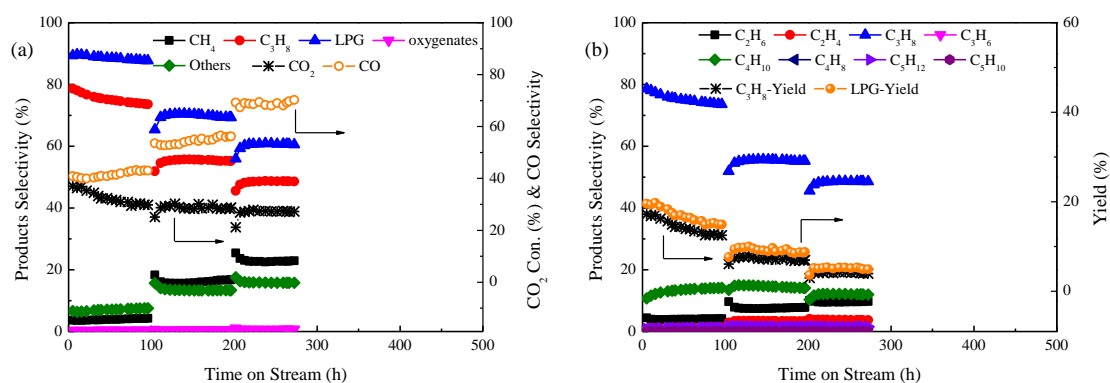
Supplementary Fig. 10. Catalytic performance for CO₂ hydrogenation. Influence of the integration manner of GaZrO_x(0.5) oxide and H-SSZ-13(6.0) zeolite on the CO₂ conversion and product distribution in direct hydrogenation of CO₂ into propane (typical reaction conditions: H₂/CO₂ = 3:1, 3.0 MPa, GHSV = 2400 mL/(g·h) and 350 °C). Others-HC represents the selectivity of hydrocarbons, excluding the methane, propane and butane.



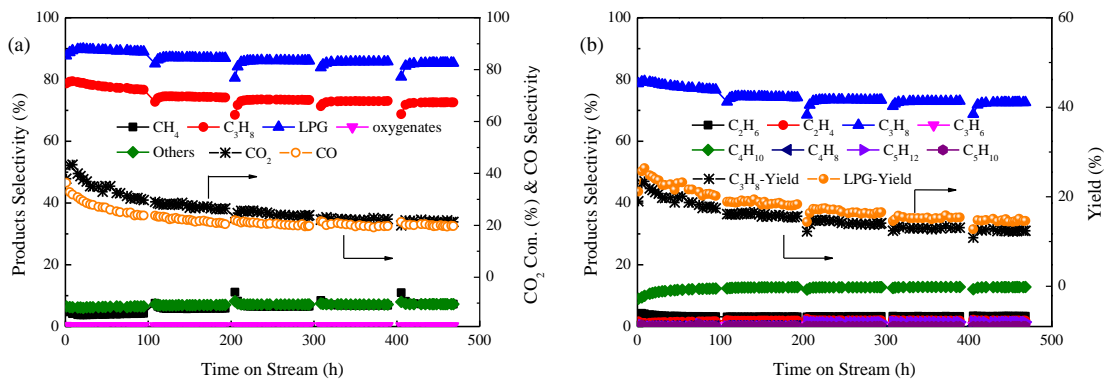
Supplementary Fig. 11. Catalytic stability. Catalytic stability test for direct conversion of CO₂ into propane over GaZrO_x(0.5)/H-SSZ-13(6.0) composite catalyst at 3.0 MPa, 350 °C, H₂/CO₂ = 6:1 and GHSV = 1000 mL/(g·h). Others-HC represents the selectivity of hydrocarbons, excluding the methane, propane and butane.



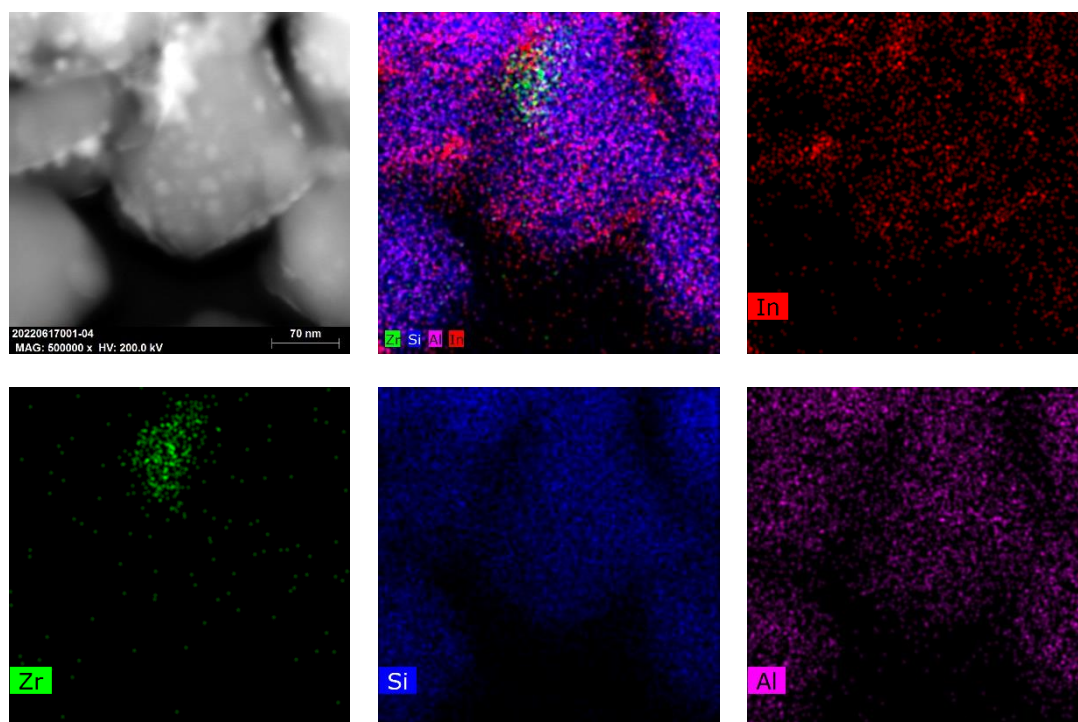
Supplementary Fig. 12. Catalytic stability. Catalytic results of InZrO_x/H-SSZ-13(6.0) for CO₂ hydrogenation to propane within 5 recycles (InZrO_x/H-SSZ-13(6.0) was regenerated at 550 °C for 2 h in H₂ after catalyzing the reaction for 100 h in each run). Reaction conditions: H₂/CO₂ = 6/1, 350 °C, 3.0 MPa and GHSV = 960 mL/g·h.



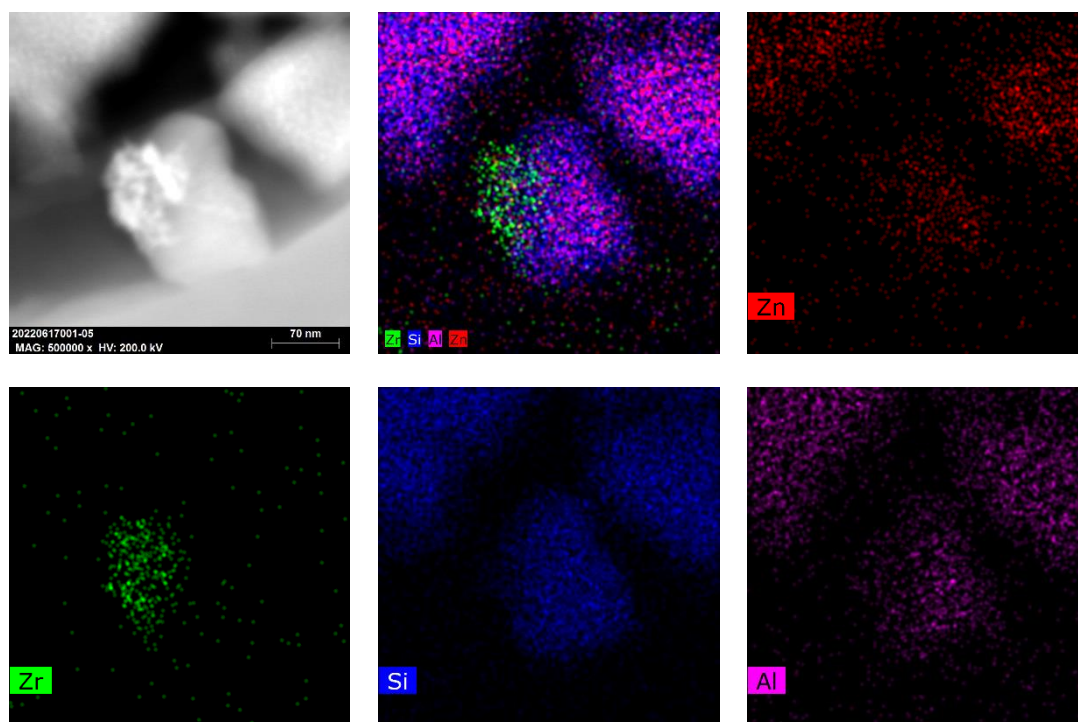
Supplementary Fig. 13. Catalytic stability. Catalytic results of ZnZrO_x/H-SSZ-13(6.0) for CO₂ hydrogenation to propane within 3 recycles (ZnZrO_x/H-SSZ-13(6.0) was regenerated at 550 °C for 2 h in H₂ after catalyzing the reaction for 100 h in each run). Reaction conditions: H₂/CO₂ = 6/1, 350 °C, 3.0 MPa and GHSV = 960 mL/g·h.



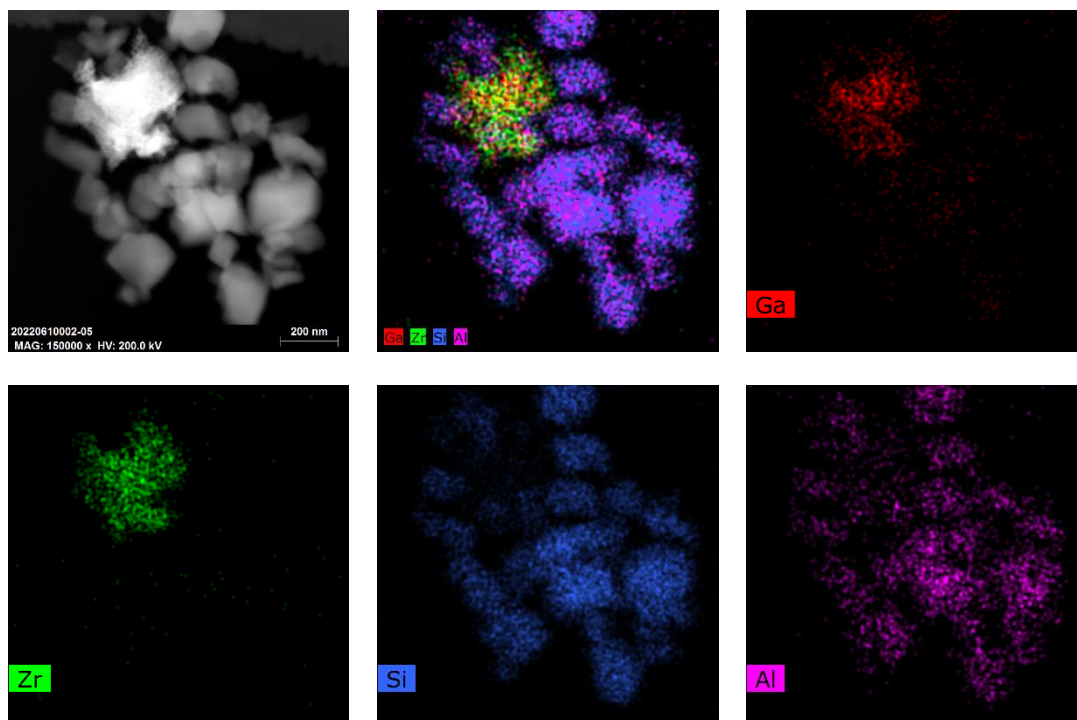
Supplementary Fig. 14. Catalytic stability. Catalytic results of GaZrO_x(0.5)/H-SSZ-13(6.0) for CO₂ hydrogenation to propane within 5 recycles (GaZrO_x(0.5)/H-SSZ-13(6.0) was regenerated at 550 °C for 2 h in H₂ after catalyzing the reaction for 100 h in each run). Reaction conditions: H₂/CO₂ = 6/1, 350 °C, 3.0 MPa and GHSV = 960 mL/g·h.



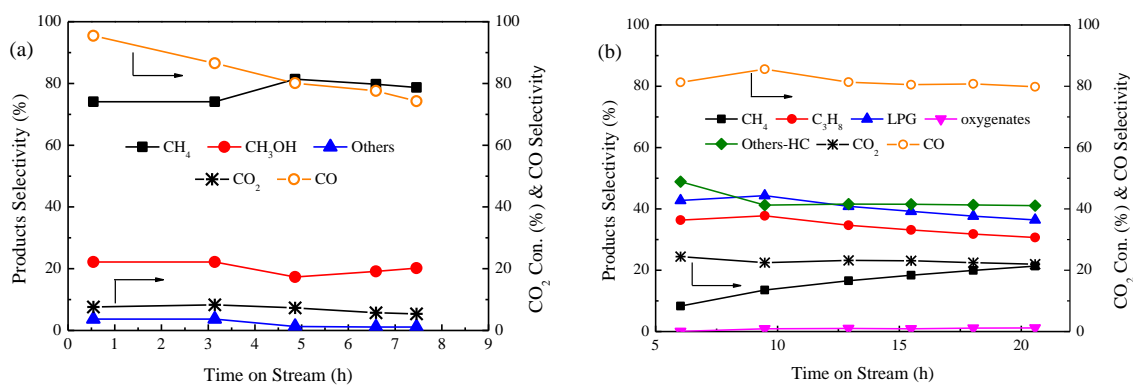
Supplementary Fig. 15. Elemental distributions. STEM-EDX elemental mappings of InZrO_x/H-SSZ-13 for CO₂ hydrogenation to propane after 5 recycles (~500 h) at 350 °C, 3.0 MPa and H₂/CO₂ = 6/1.



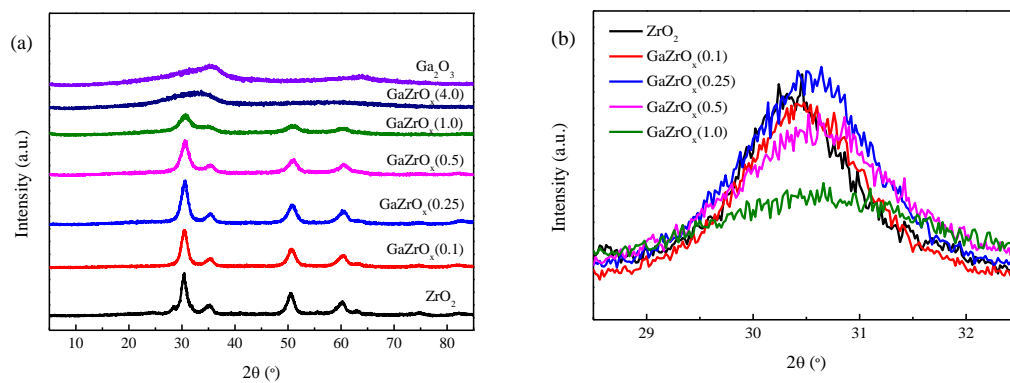
Supplementary Fig. 16. Elemental distribution. STEM-EDX elemental mappings of $\text{ZnZrO}_x/\text{H-SSZ-13}$ for CO_2 hydrogenation to propane after 3 recycles (~ 300 h) at 350°C , 3.0 MPa and $\text{H}_2/\text{CO}_2 = 6/1$.



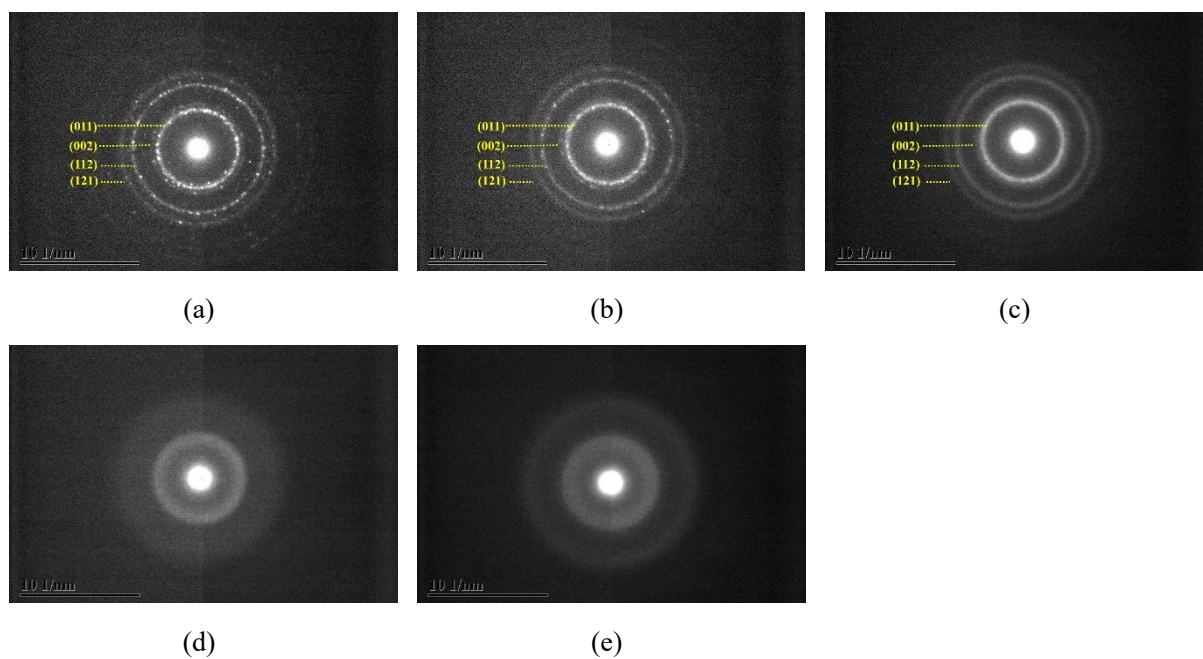
Supplementary Fig. 17. Elemental distribution. STEM-EDX elemental mappings of GaZrO_x/H-SSZ-13 for CO₂ hydrogenation to propane after 5 recycles (~500 h) at 350 °C, 3.0 MPa and H₂/CO₂ = 6/1.



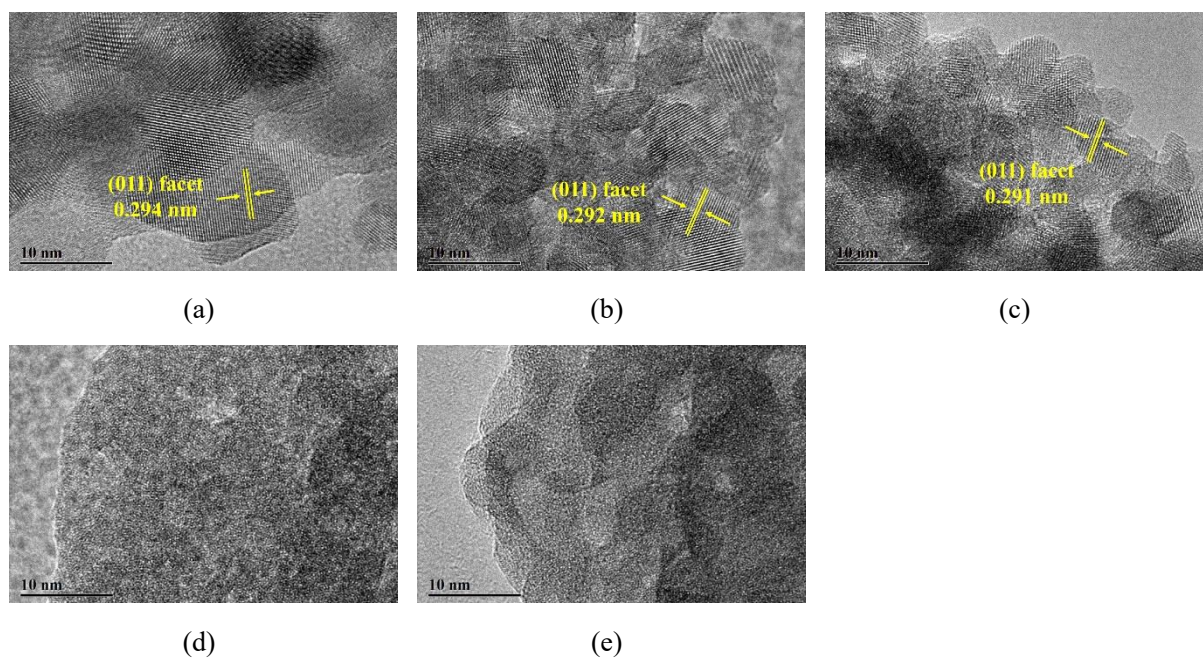
Supplementary Fig. 18. Catalytic performance for CO₂ hydrogenation. CO₂ conversion and product selectivity on CuZrO_x (a) and CuZrO_x/H-SSZ-13(6.0) (b) (reaction conditions: (a) H₂/CO₂ = 3/1, 350 °C, 3.0 MPa and GHSV = 48000 mL/g·h; (b) H₂/CO₂ = 3/1, 350 °C, 3.0 MPa and GHSV = 2400 mL/g·h).



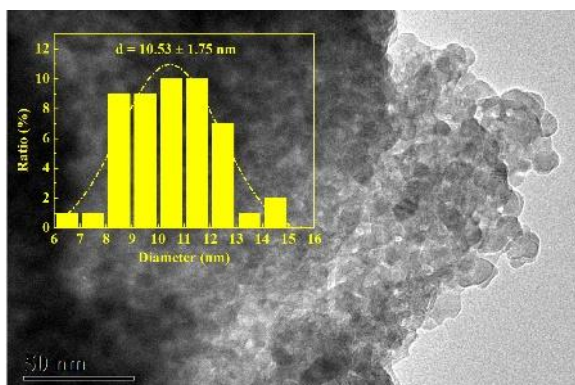
Supplementary Fig. 19. Crystal structure. XRD patterns of ZrO_2 , Ga_2O_3 and $\text{GaZrO}_x(\text{N})$ oxides with different Ga/Zr molar ratios (a) and their enlarged region in the 2θ value from 28.5° to 32.5° (b).



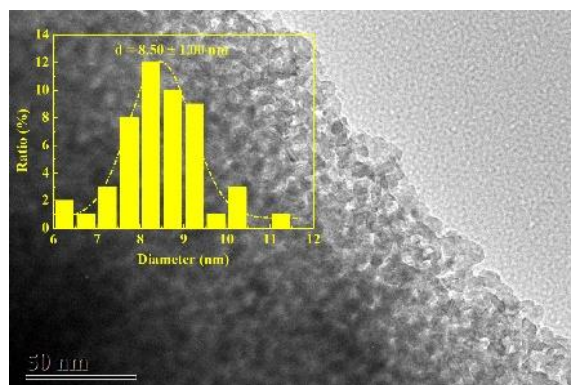
Supplementary Fig. 20. Crystal structure. Selected area electron diffraction (SAED) patterns of ZrO_2 (a), $\text{GaZrO}_x(0.1)$ (b), $\text{GaZrO}_x(0.5)$ (c), $\text{GaZrO}_x(4.0)$ (d) and Ga_2O_3 (e).



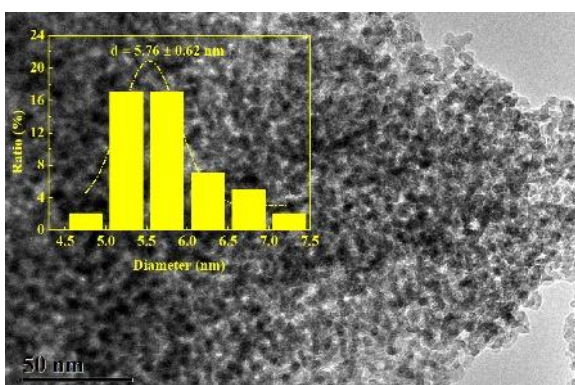
Supplementary Fig. 21. Catalyst morphology. High-resolution transmission electron microscopy (HRTEM) images of ZrO_2 (a), $\text{GaZrO}_x(0.1)$ (b), $\text{GaZrO}_x(0.5)$ (c), $\text{GaZrO}_x(4.0)$ (d) and Ga_2O_3 (e).



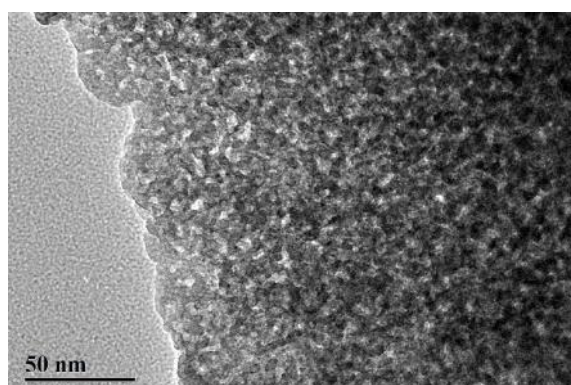
(a)



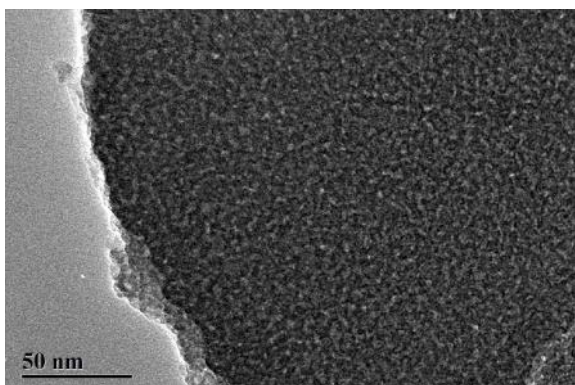
(b)



(c)

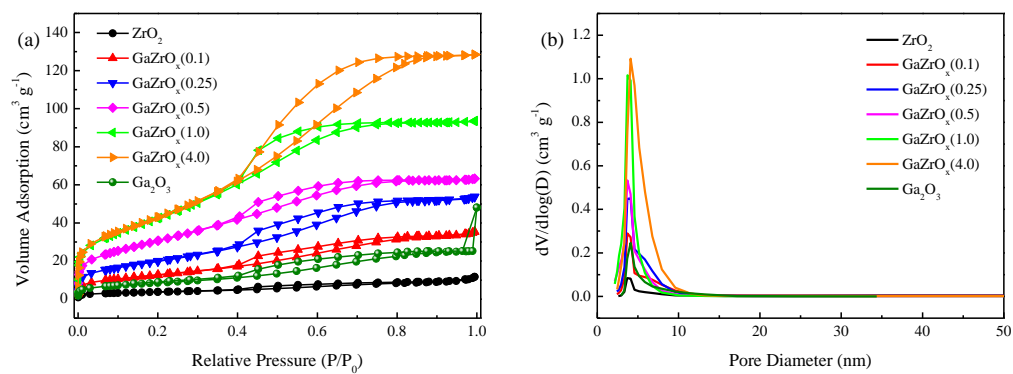


(d)

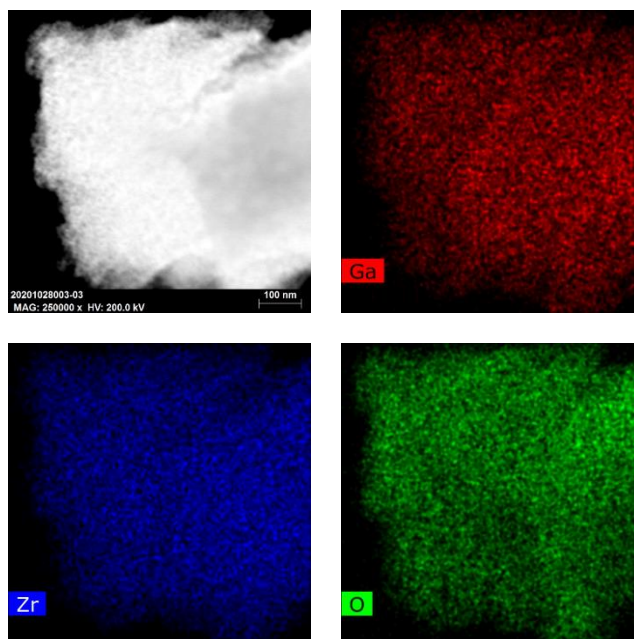


(e)

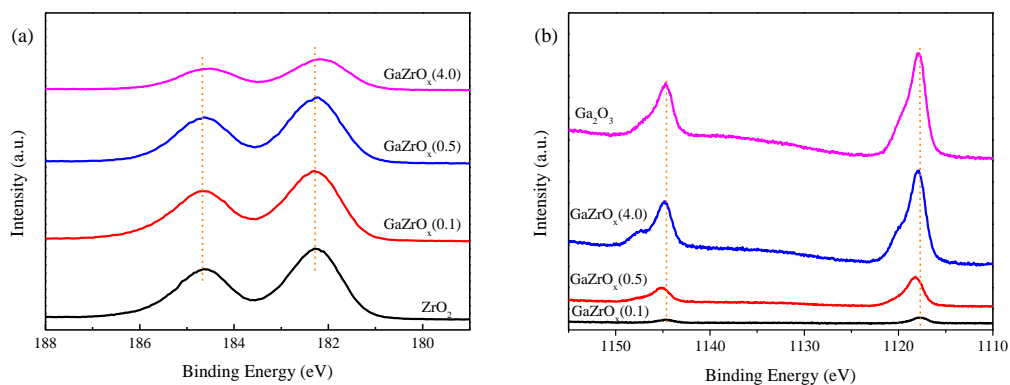
Supplementary Fig. 22. Catalyst morphology. Transmission electron microscopy (TEM) images and particles size distributions, as estimated by counting ~100 NPs, of ZrO₂ (a), GaZrO_x(0.1) (b), GaZrO_x(0.5) (c), GaZrO_x(4.0) (d) and Ga₂O₃ (e).



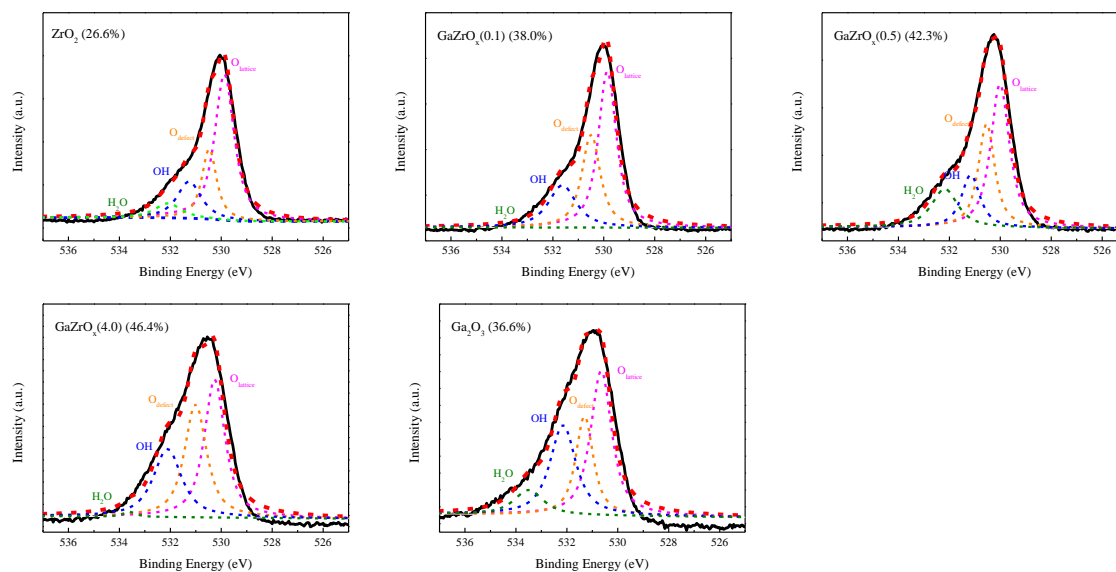
Supplementary Fig. 23. Texture properties. N₂ sorption isotherms (a) and corresponding pore size distributions (b) of ZrO₂, Ga₂O₃ and GaZrO_x(N) oxides with different Ga/Zr molar ratios.



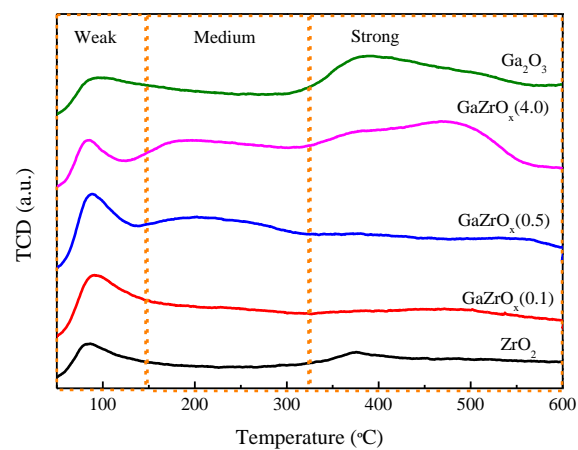
Supplementary Fig. 24. Morphology and elemental distribution. Scanning transmission electron microscopy (STEM) image and energy-dispersive X-ray (EDX) elemental mappings of $\text{GaZrO}_x(0.5)$ oxide.



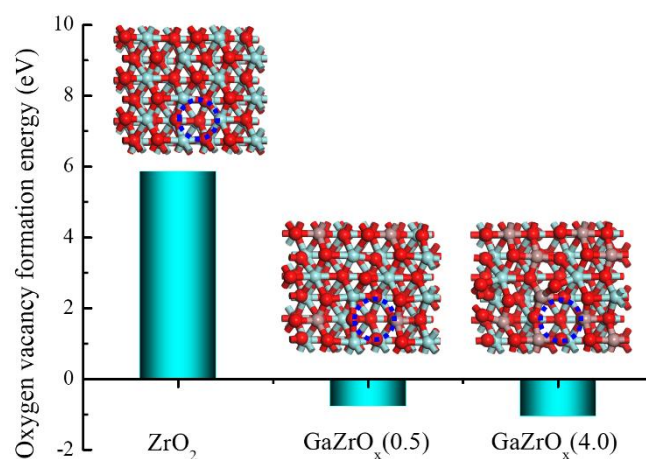
Supplementary Fig. 25. Surface electronic properties. Zr(3d) (a) and Ga(2p) (b) x-ray photoelectron spectra (XPS) of ZrO_2 , Ga_2O_3 and $GaZrO_x(N)$ oxides with different Ga/Zr molar ratios.



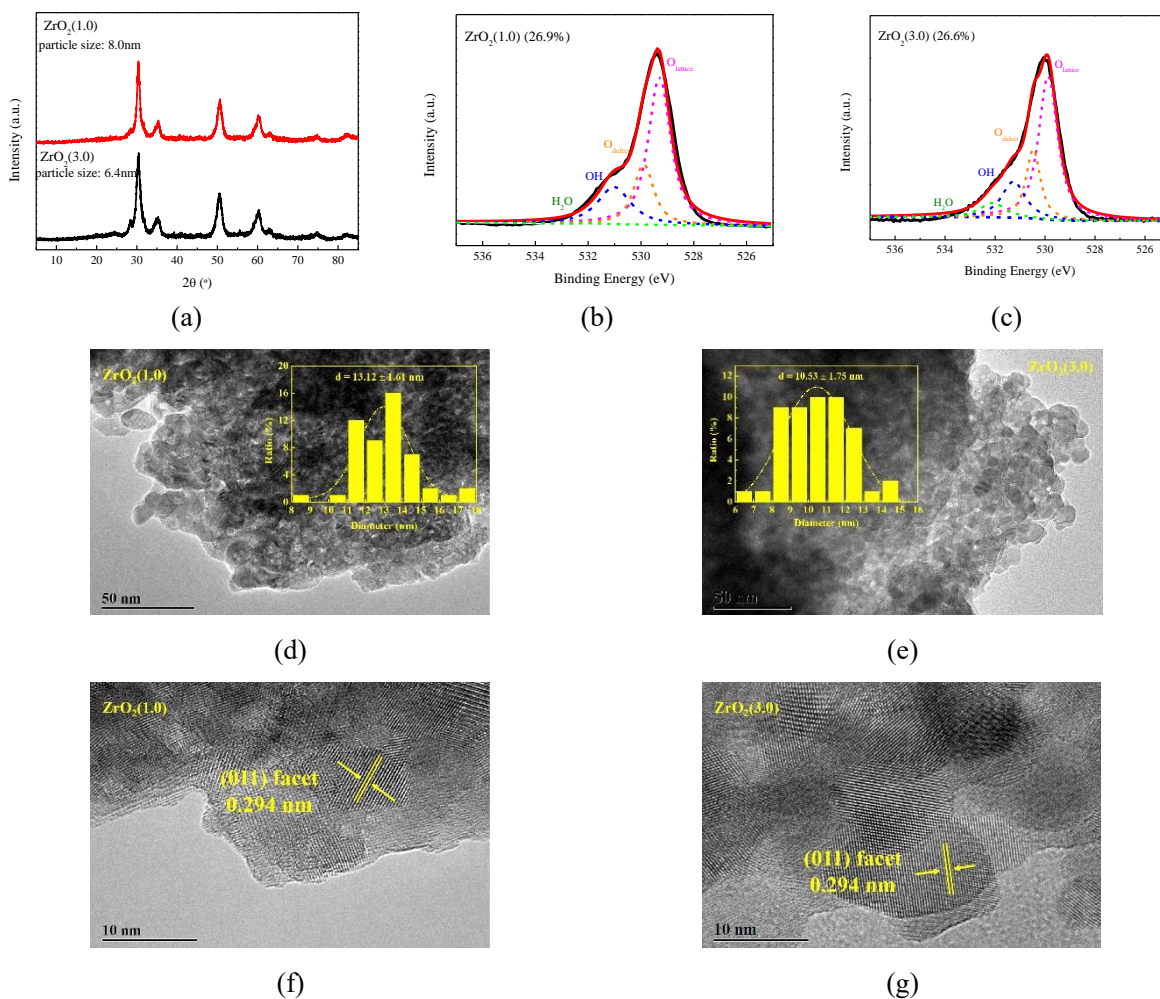
Supplementary Fig. 26. Concentration of surface oxygen vacancies. O(1s) XPS of ZrO₂, Ga₂O₃ and GaZrO_x(N) oxides with different Ga/Zr molar ratios. The data represent the concentrations of surface oxygen vacancies (O_v), as calculated by the method reported in Ref [1,2].



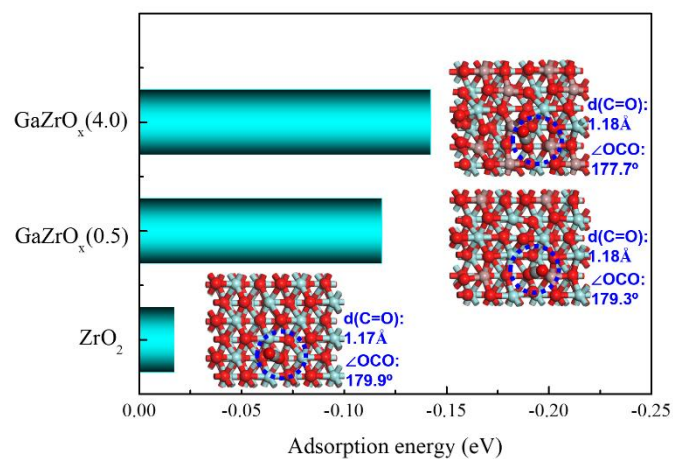
Supplementary Fig. 27. CO₂-TPD profiles of ZrO₂, Ga₂O₃ and GaZrO_x(N) oxides with different Ga/Zr molar ratios.



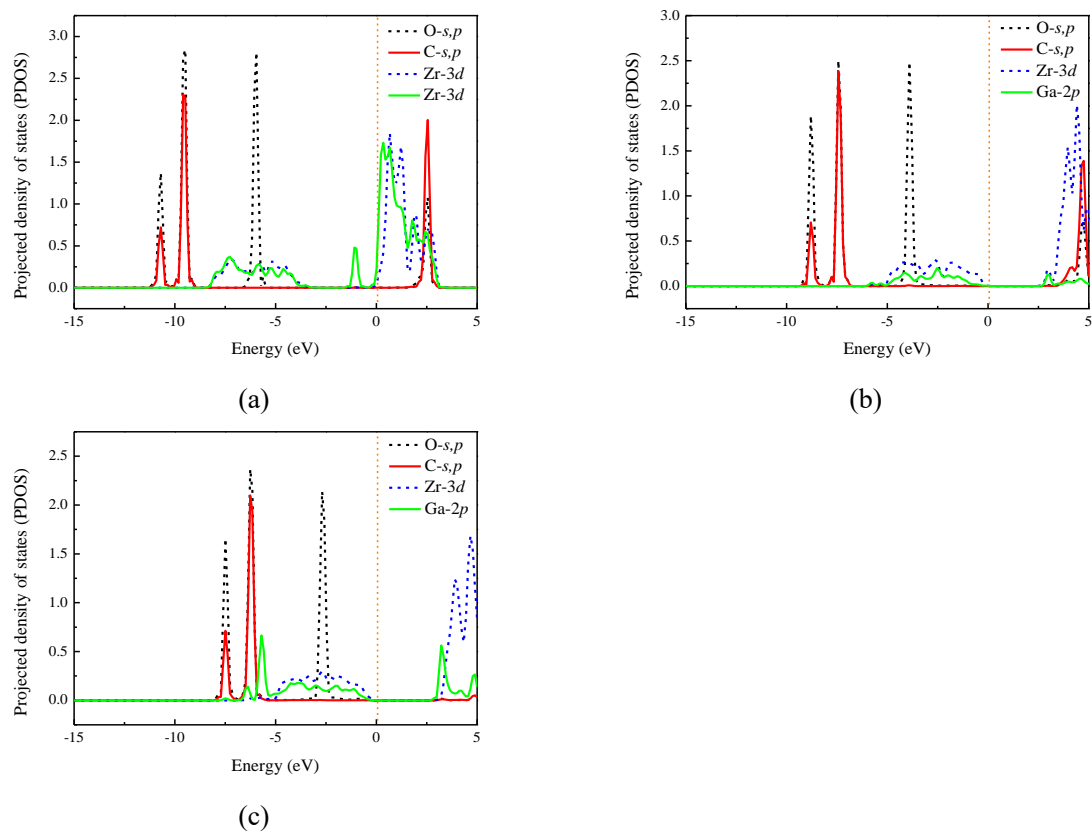
Supplementary Fig. 28. Oxygen vacancy formation energy. Calculated oxygen vacancy formation energies on ZrO₂, GaZrO_x(0.5) and GaZrO_x(4.0) model systems (insert: optimized models of ZrO₂, GaZrO_x(0.5) and GaZrO_x(4.0) (blue cycle represents the oxygen defects (atom coloring: red (O), blue (Zr) and erythrinus (Ga)).



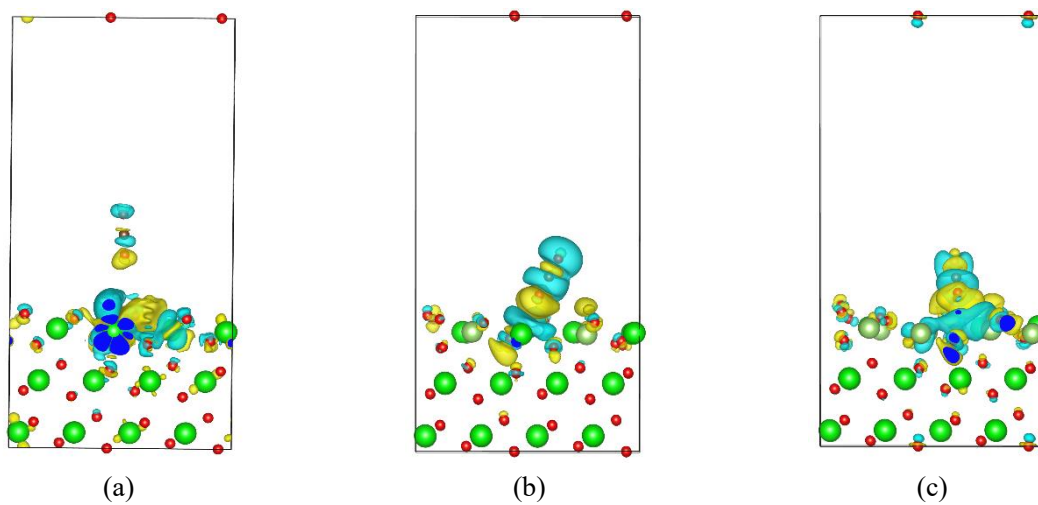
Supplementary Fig. 29. Structure and property of various ZrO_2 . XRD patterns (a), O(1s)-XPS (b and c), TEM images (insert: particle size distribution) (d and e) and HRTEM images (f and g) of $\text{ZrO}_2(1.0)$ and $\text{ZrO}_2(3.0)$ that are prepared by the sol-gel method with the glucose/ Zr^{4+} molar ratio of 1.0 and 3.0 respectively.



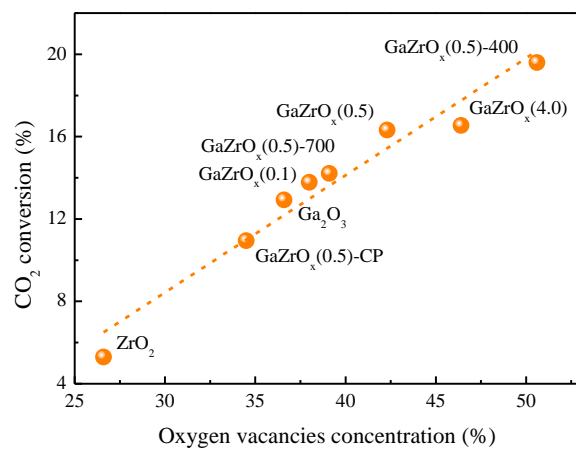
Supplementary Fig. 30. CO₂ adsorption energy. Calculated CO₂ adsorption energies and corresponding optimized adsorption configurations on ZrO₂, GaZrO_x(0.5) and GaZrO_x(4.0) model systems (atom coloring: red (O), blue (Zr), erythrinus (Ga) and grey (C)).



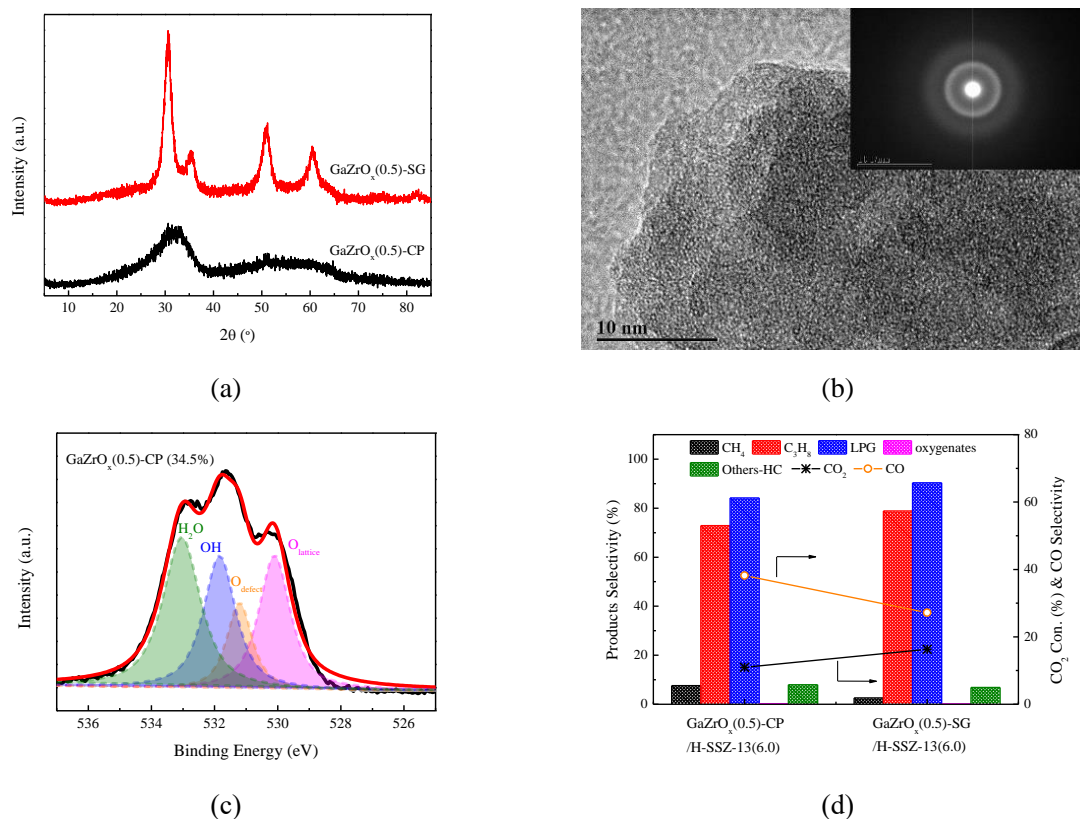
Supplementary Fig. 31. Projected density of states (PDOS). The PDOS results of O and C atoms of CO_2 , and Zr and Ga atoms of ZrO_2 (a), $\text{GaZrO}_x(0.5)$ (b) and $\text{GaZrO}_x(4.0)$ (c) models for CO_2 adsorption.



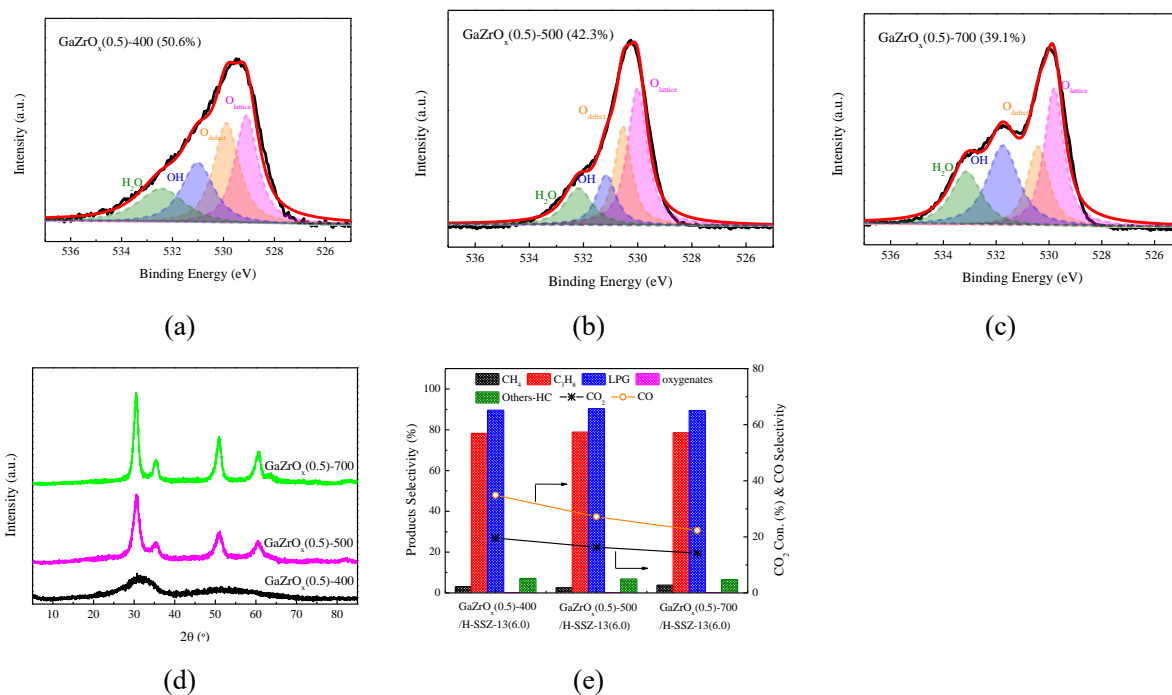
Supplementary Fig. 32. Charge difference density (CDD). The CDD results for CO₂ adsorption on ZrO₂ (a), GaZrO_x(0.5) (b) and GaZrO_x(4.0) (c) models (the accumulation and depletion charge regions are shown in yellow and cyan respectively).



Supplementary Fig. 33. Dependence of CO₂ conversion on the surface oxygen vacancy concentration, as estimated by the O(1s) XPS, of ZrO₂ and GaZrO_x(N) oxides.

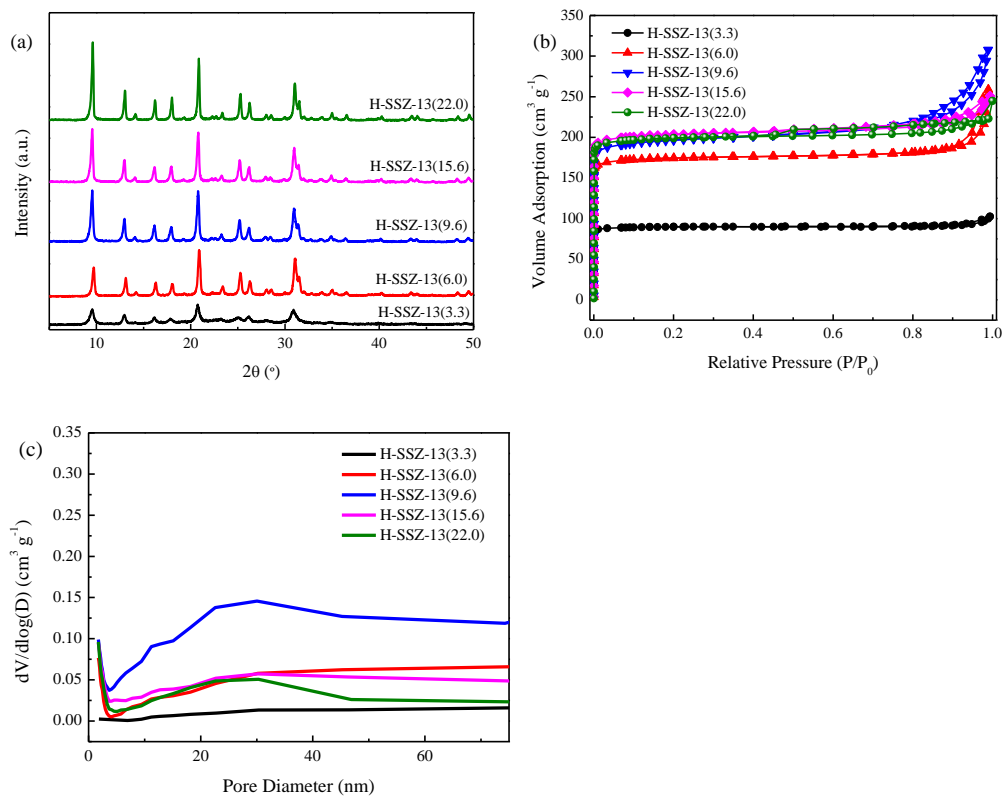


Supplementary Fig. 34. Structure and performance of various GaZrO_x(0.5) catalysts. (a) XRD patterns of GaZrO_x(0.5)-SG and GaZrO_x(0.5)-CP, (b) HRTEM image (insert: SAED pattern) and (c) O(1s)-XPS of GaZrO_x(0.5)-CP, and (d) the catalytic results of GaZrO_x(0.5)-SG/H-SSZ-13(6.0) and GaZrO_x(0.5)-CP/H-SSZ-13(6.0) for hydrogenation of CO₂ into propane (typical reaction conditions: H₂/CO₂ = 3:1, 3.0 MPa, GHSV = 2400 mL/(g·h) and 350 °C). Others-HC refers to the selectivity of hydrocarbons with methane, propane and butane excluded. GaZrO_x(0.5)-CP and GaZrO_x(0.5)-SG were prepared by the co-precipitation and sol-gel methods respectively.

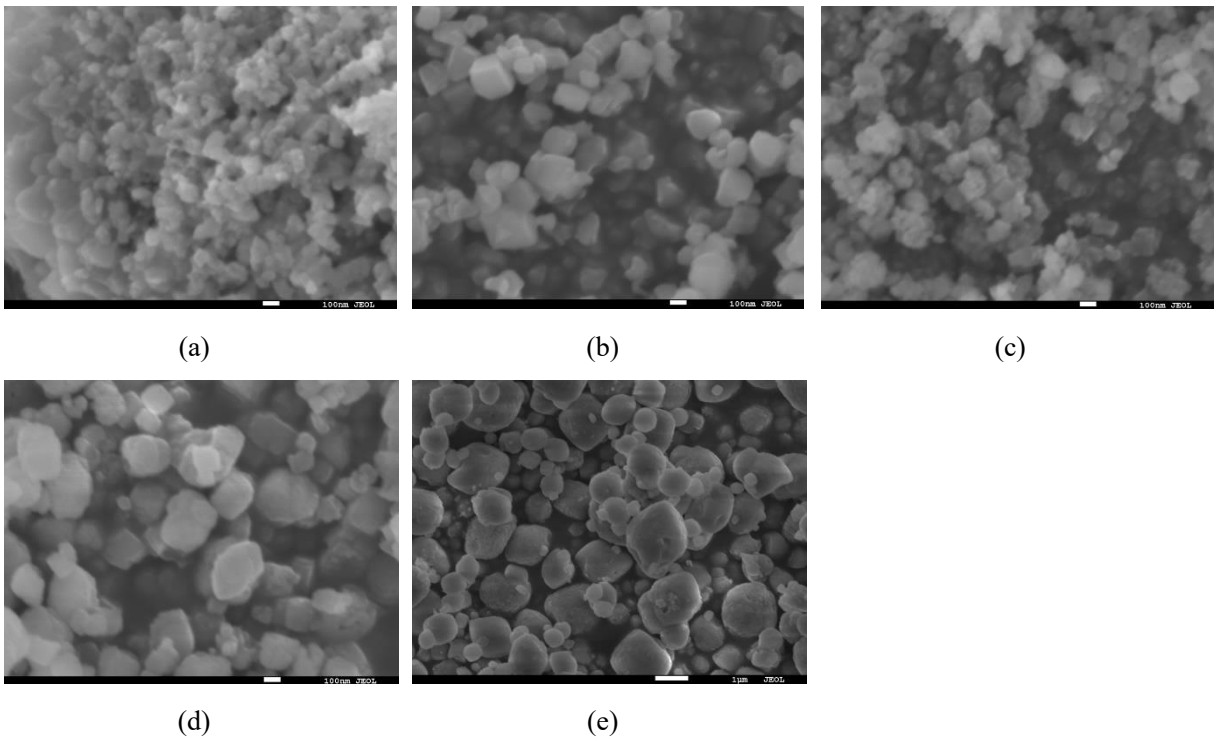


Supplementary Fig. 35. Structure and performance of various GaZrO_x(0.5) catalysts.

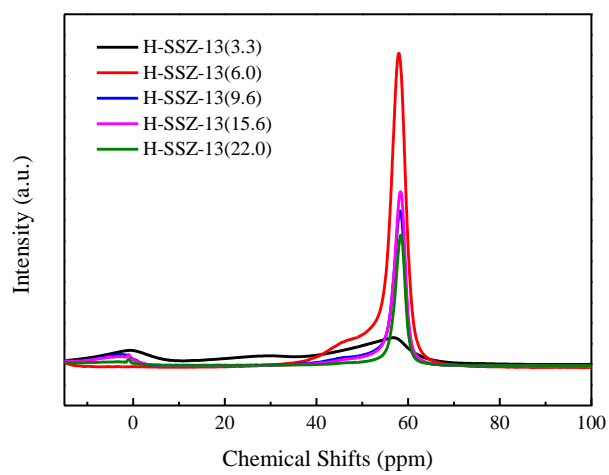
O(1s)-XPS (a-c) and XRD patterns (d) of GaZrO_x(0.5)-400, GaZrO_x(0.5)-500 and GaZrO_x(0.5)-700, and the catalytic results (e) of GaZrO_x(0.5)-400/H-SSZ-13(6.0), GaZrO_x(0.5)-500/H-SSZ-13(6.0) and GaZrO_x(0.5)-700/H-SSZ-13(6.0) for hydrogenation of CO₂ into propane (typical reaction conditions: H₂/CO₂ = 3:1, 3.0 MPa, GHSV = 2400 mL/(g·h) and 350 °C). Others-HC refers to the selectivity of hydrocarbons with methane, propane and butane excluded. GaZrO_x(0.5)-400, GaZrO_x(0.5)-500 and GaZrO_x(0.5)-700 prepared by the sol-gel method were calcined at 400 °C, 500 °C and 700 °C, respectively.



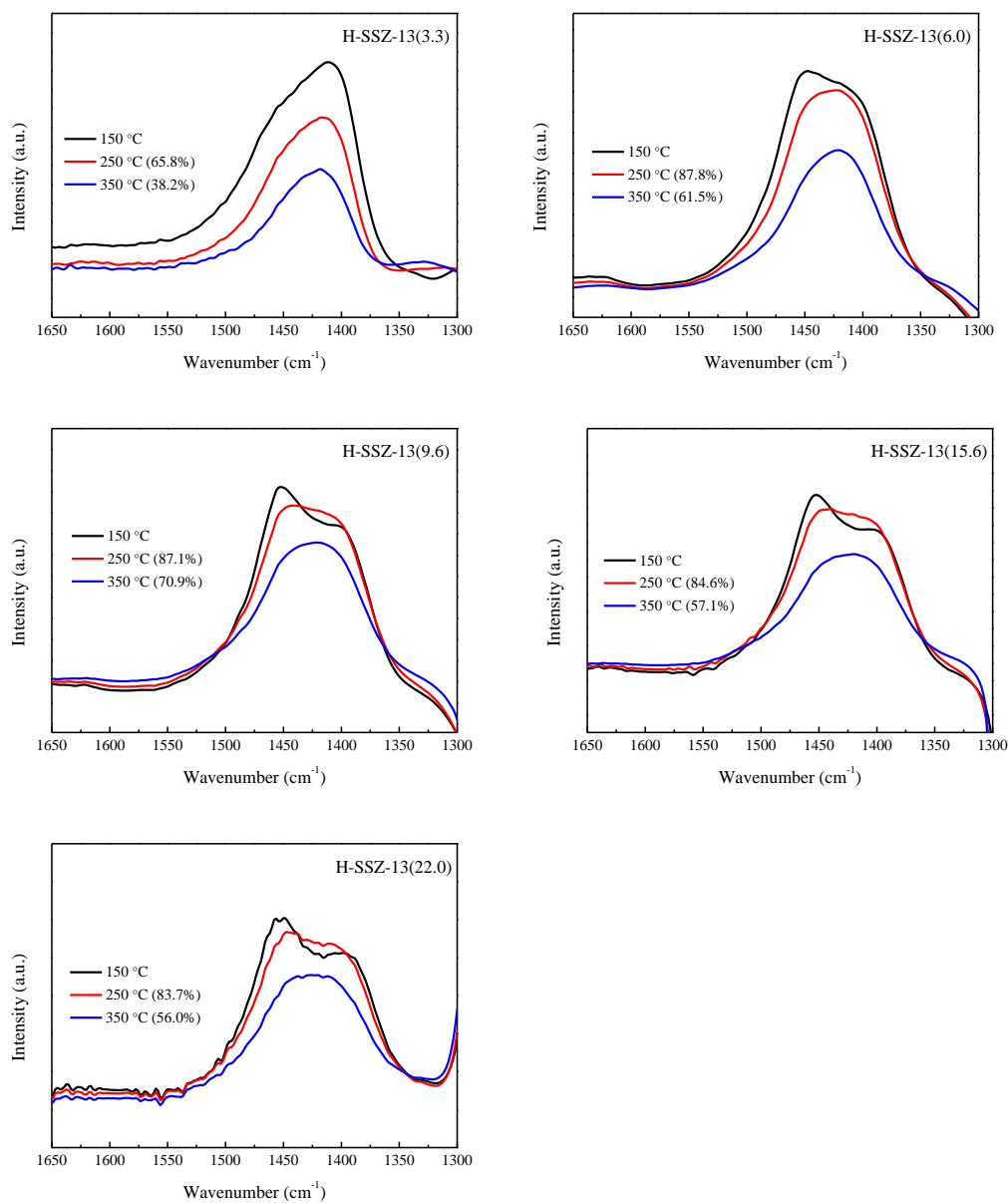
Supplementary Fig. 36. Crystal structure and texture property of various zeolites. XRD patterns (a), N_2 sorption isotherms (b) and corresponding pore size distributions (c) of H-SSZ-13 zeolites with different Si/Al ratios.



Supplementary Fig. 37. Morphology of various zeolites. SEM images of H-SSZ-13 zeolites with Si/Al ratio of 3.3 (a), 6.0 (b), 9.6 (c), 15.6 (d) and 22.0 (e).

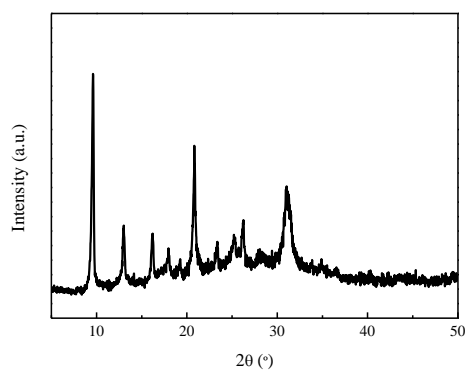


Supplementary Fig. 38. ^{27}Al MAS NMR spectra of H-SSZ-13 zeolites with different Si/Al ratios.

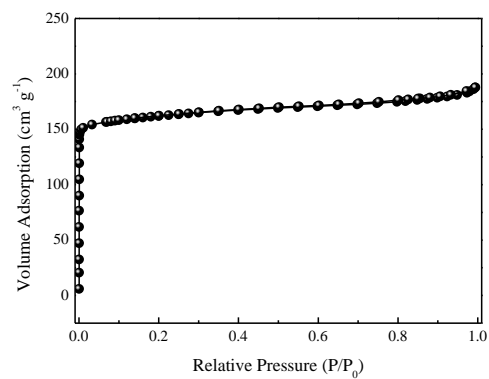


Supplementary Fig. 39. NH₃-IR spectra of H-SSZ-13 zeolites with different Si/Al ratios.

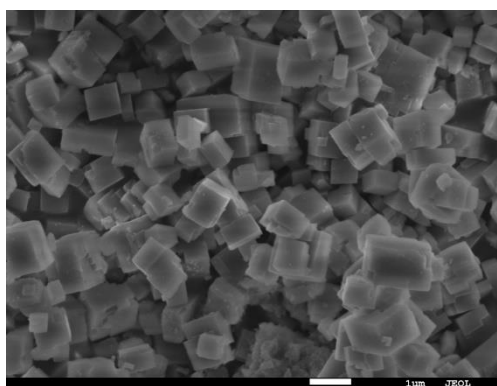
The data in the parentheses represent the proportion of medium (250 °C) and strong (350 °C) Brønsted acid sites to the total Brønsted acid sites (150 °C), as calculated by the peak areas at around 1430 cm⁻¹ collected at 150, 250 °C and 350 °C.³



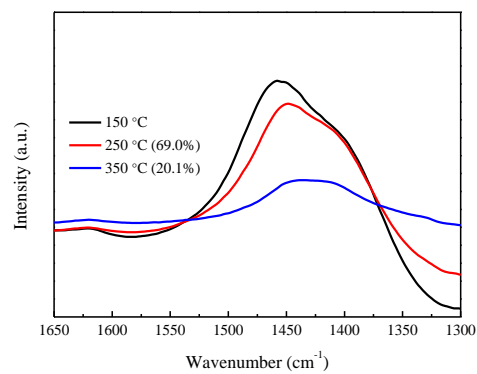
(a)



(b)



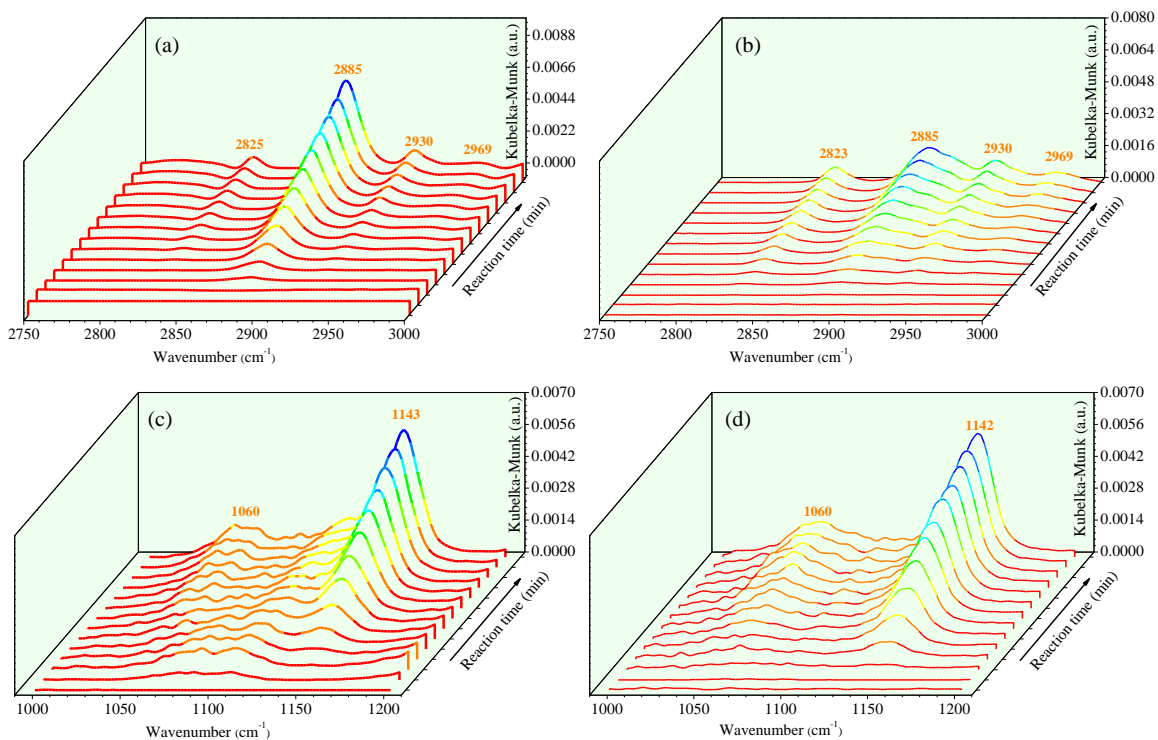
(c)



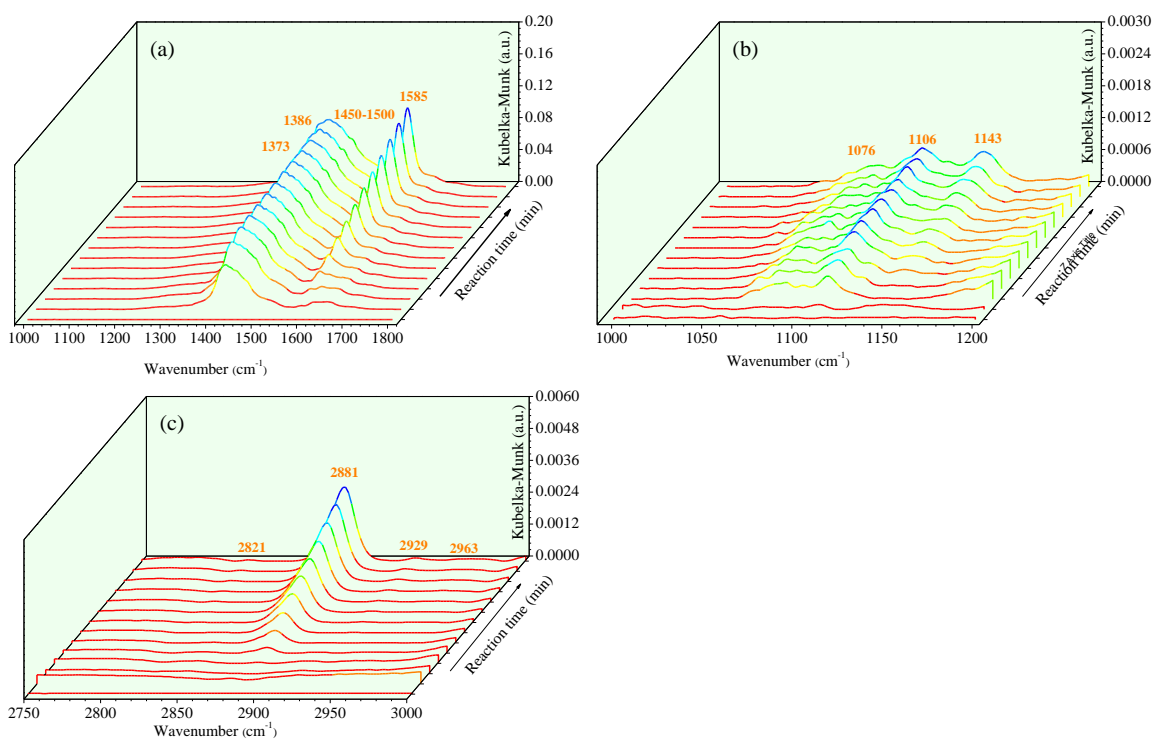
(d)

Supplementary Fig. 40. Structure, morphology and acidic property of H-SAPO-34.

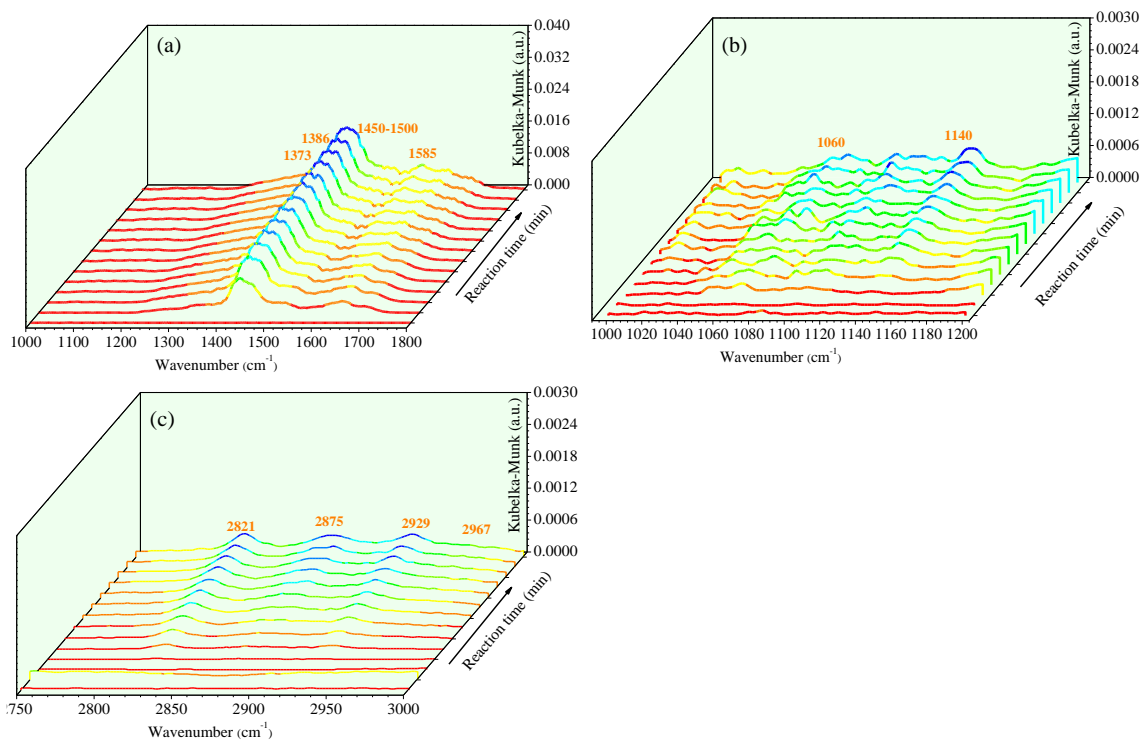
XRD pattern (a), N₂ sorption isotherms (b), SEM image (c) and NH₃-IR spectra (d) of H-SAPO-34 zeolite.



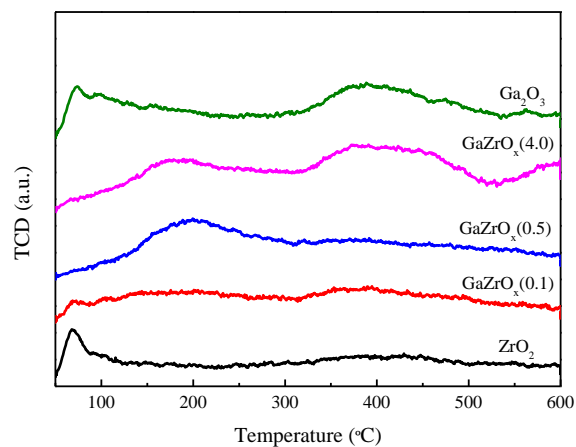
Supplementary Fig. 41. In situ spectroscopy. Time-dependent DRIFT spectra for CO₂ hydrogenation to methanol on GaZrO_x(0.5) (a and c) and GaZrO_x(4.0) (b and d). The spectra were collected every 5 min up to 60 min after pre-treatment of the sample with H₂ (30 mL/min) for 2 h at 400 °C and purged with Ar (30 mL/min) for 0.5 h at 300 °C (typical reaction conditions: 300 °C and 0.1 MPa). The arrow represents the direction of time evolution.



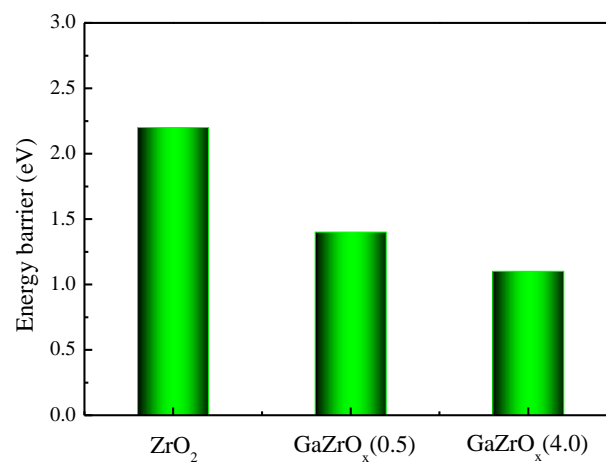
Supplementary Fig. 42. In situ spectroscopy. Time-dependent DRIFT spectra for CO₂ hydrogenation to methanol on GaZrO_x(0.1) oxide. The spectra were collected every 5 min up to 60 min after pre-treatment of the sample with H₂ (30 mL/min) for 2 h at 400 °C and purged with Ar (30 mL/min) for 0.5 h at 300 °C (typical reaction conditions: 300 °C and 0.1 MPa). The arrow represents the direction of time evolution.



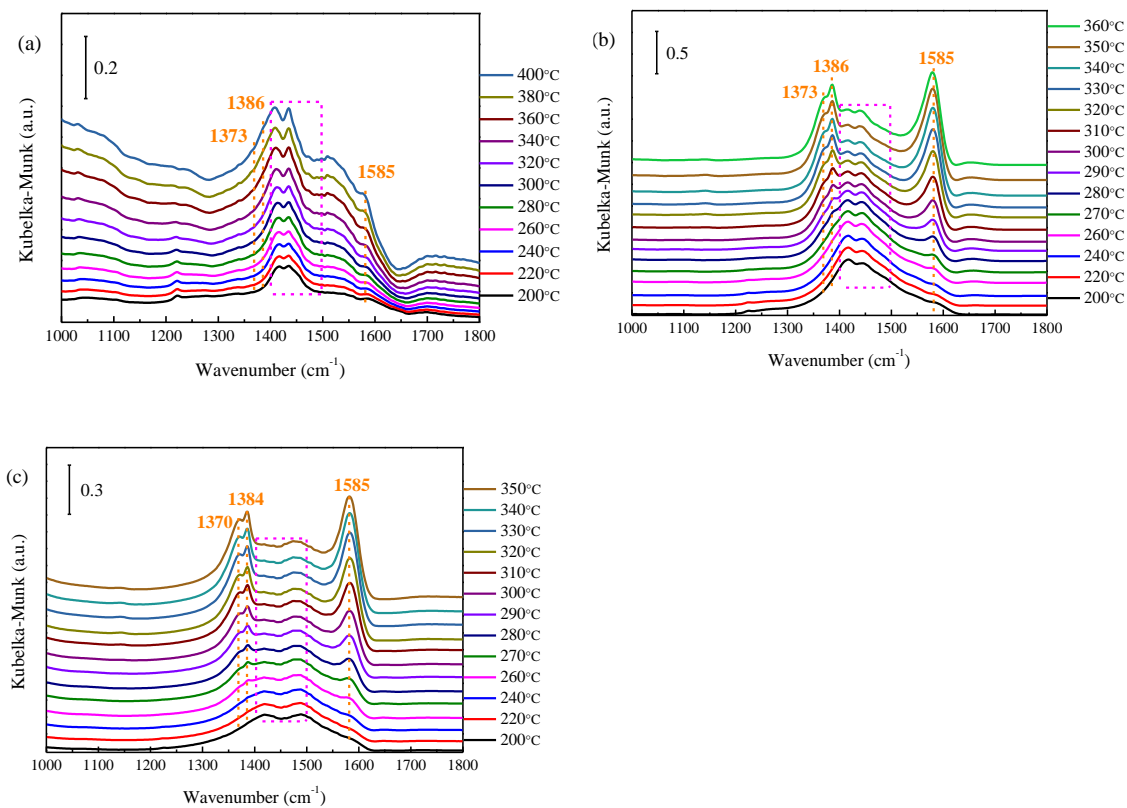
Supplementary Fig. 43. In situ spectroscopy. Time-dependent DRIFT spectra for CO₂ hydrogenation to methanol on ZrO₂ oxide. The spectra were collected every 5 min up to 60 min after pre-treatment of the sample with H₂ (30 mL/min) for 2 h at 400 °C and purged with Ar (30 mL/min) for 0.5 h at 300 °C (typical reaction conditions: 300 °C and 0.1 MPa). The arrow represents the direction of time evolution.



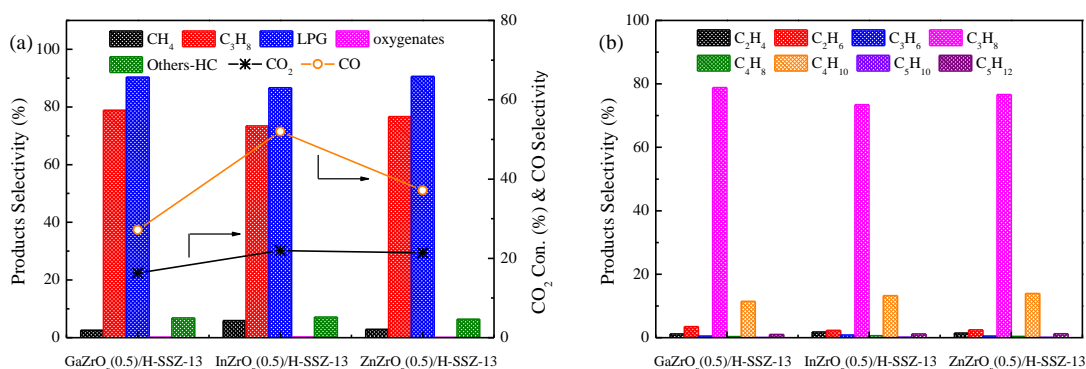
Supplementary Fig. 44. H₂-TPD profiles of ZrO₂, Ga₂O₃ and GaZrO_x(N) oxides with different Ga/Zr molar ratios.



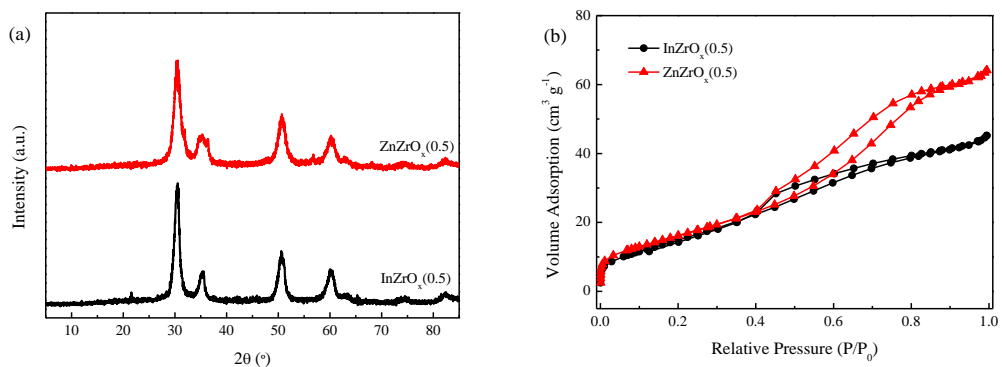
Supplementary Fig. 45. H₂ dissociation. Calculated energy barriers for dissociation of H₂ on ZrO₂, GaZrO_x(0.5) and GaZrO_x(4.0).



Supplementary Fig. 46. In situ spectroscopy. Temperature-dependent in situ DRIFT spectra for CO₂ hydrogenation to methanol at different temperature on ZrO₂ (a), GaZrO_x(0.5) (b) and GaZrO_x(4.0) (c).

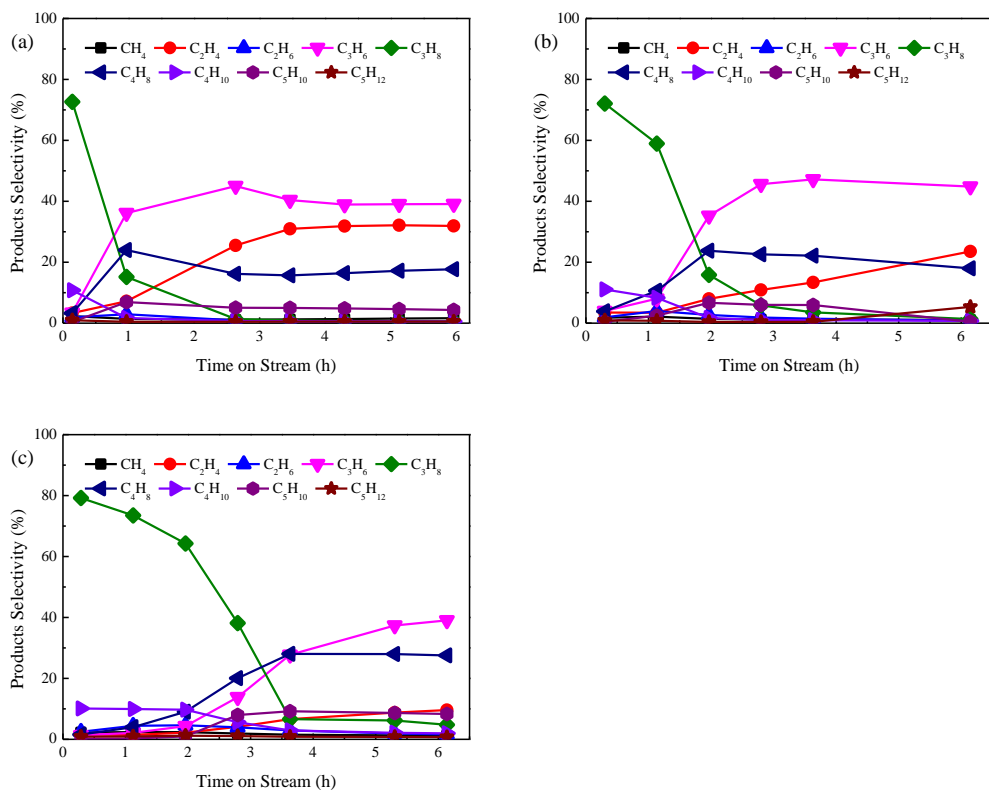


Supplementary Fig. 47. Catalytic performance for CO₂ hydrogenation. Catalytic results for direct hydrogenation of CO₂ into propane over bifunctional catalyst system consisting of various metal oxides and H-SSZ-13(6.0) zeolite (typical reaction conditions: H₂/CO₂ = 3:1, GHSV = 2400 mL/(g·h), 3.0 MPa and 350 °C). Others-HC represents the selectivity of hydrocarbons, excluding methane, propane and butane.

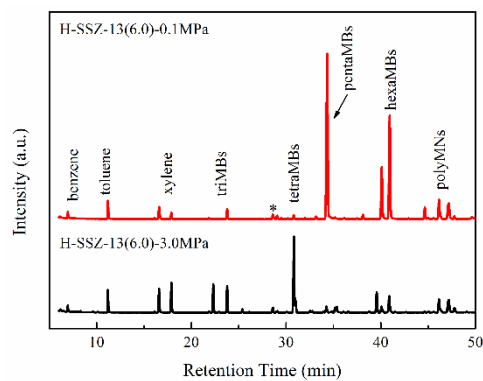


Supplementary Fig. 48. Structure and property of $\text{ZnZrO}_x(0.5)$ and $\text{InZrO}_x(0.5)$ oxides.

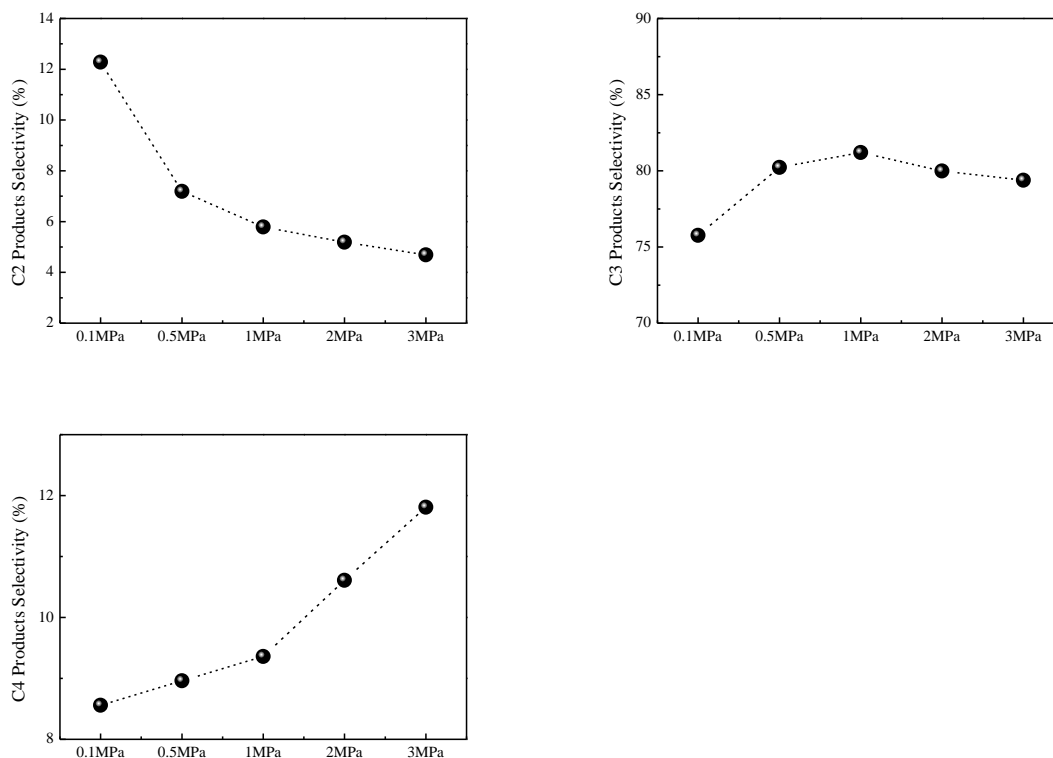
XRD patterns (a) and N_2 sorption profiles (b) of $\text{ZnZrO}_x(0.5)$ and $\text{InZrO}_x(0.5)$ oxides (the molar ratio of Zn/Zr or In/Zr is 0.5).



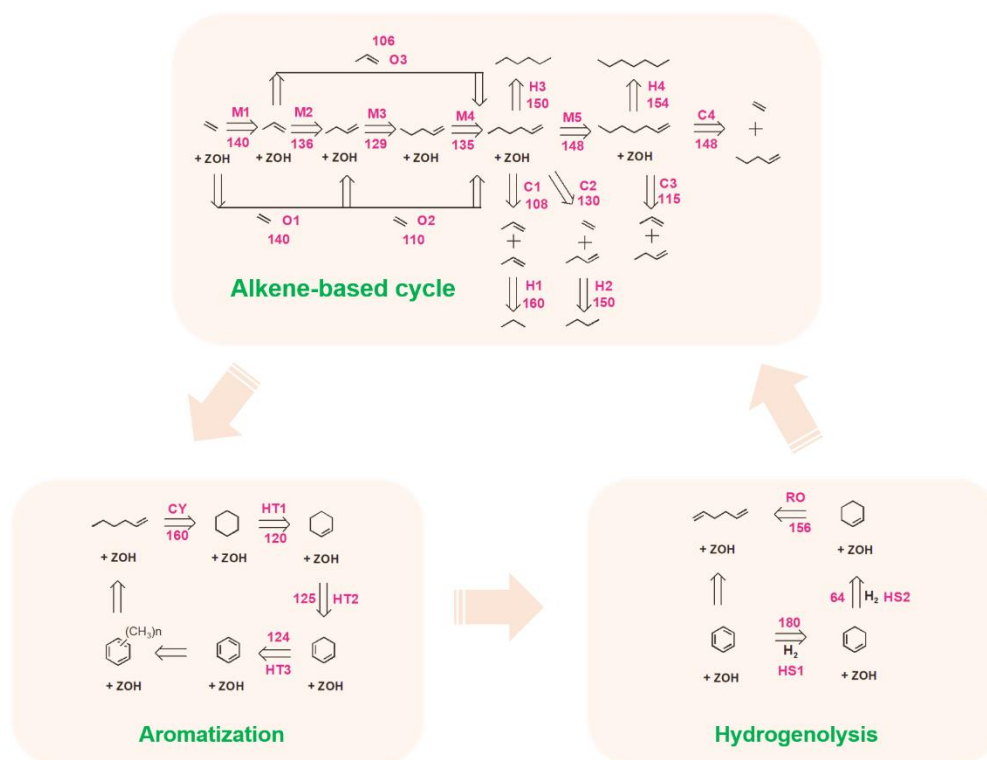
Supplementary Fig. 49. Catalytic performance for methanol conversion. Catalytic results for methanol conversion on H-SSZ-13(6.0) zeolite in H₂ atmosphere at 0.1 MPa, 350 °C and WHSV_{methanol} of 2.0 h⁻¹ (a), WHSV_{methanol} of 1.0 h⁻¹ (b) and WHSV_{methanol} of 0.5 h⁻¹ (c).



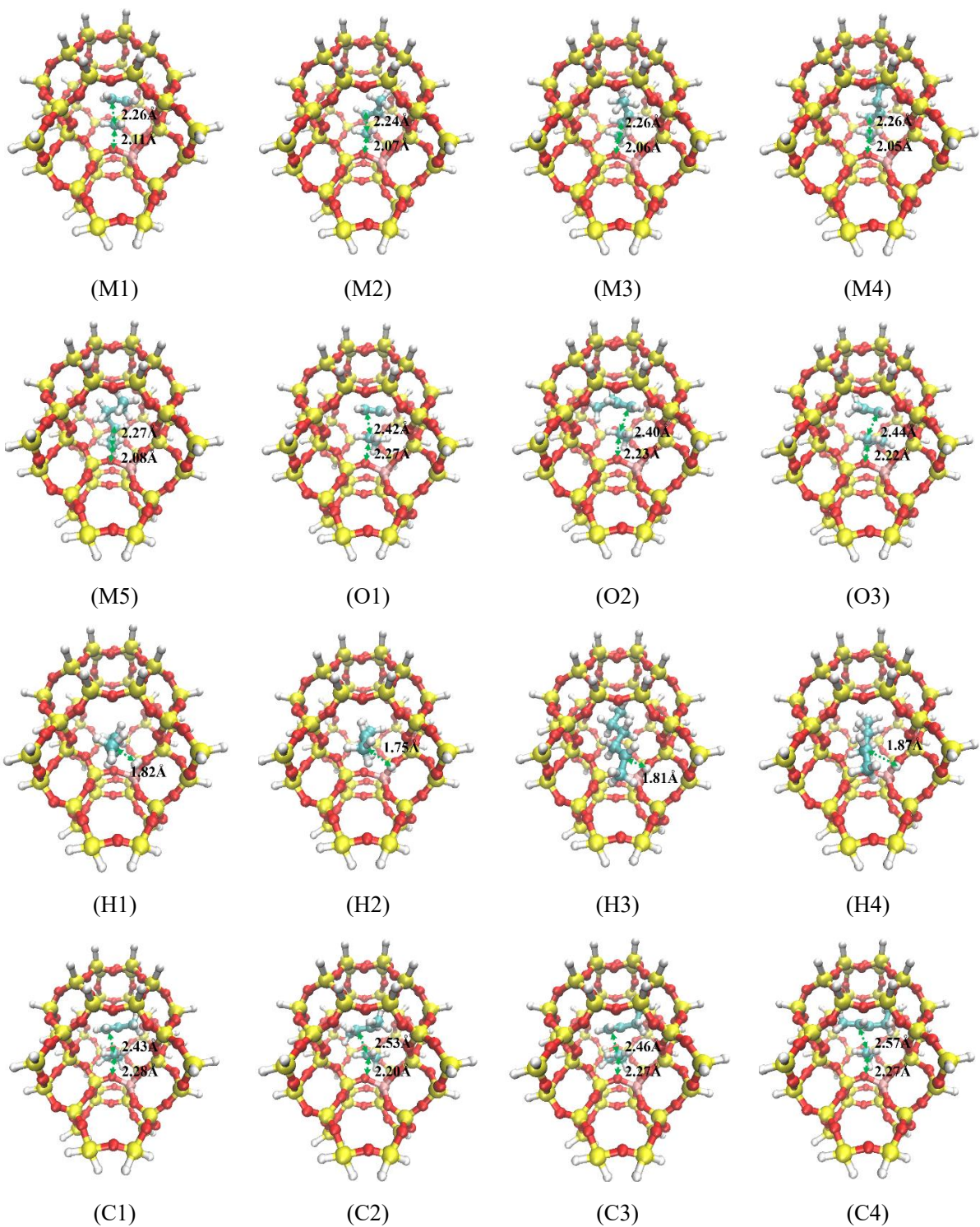
Supplementary Fig. 50. Retained species on catalysts. GC-MS diagrams of the carbonaceous species confined in the H-SSZ-13(6.0) after catalyzing methanol conversion at 350 °C, $\text{WHSV}_{\text{methanol}}$ of 0.24 h^{-1} and 0.1 MPa or 3.0 MPa in H_2 atmosphere (* is the internal standard of hexachloroethane).



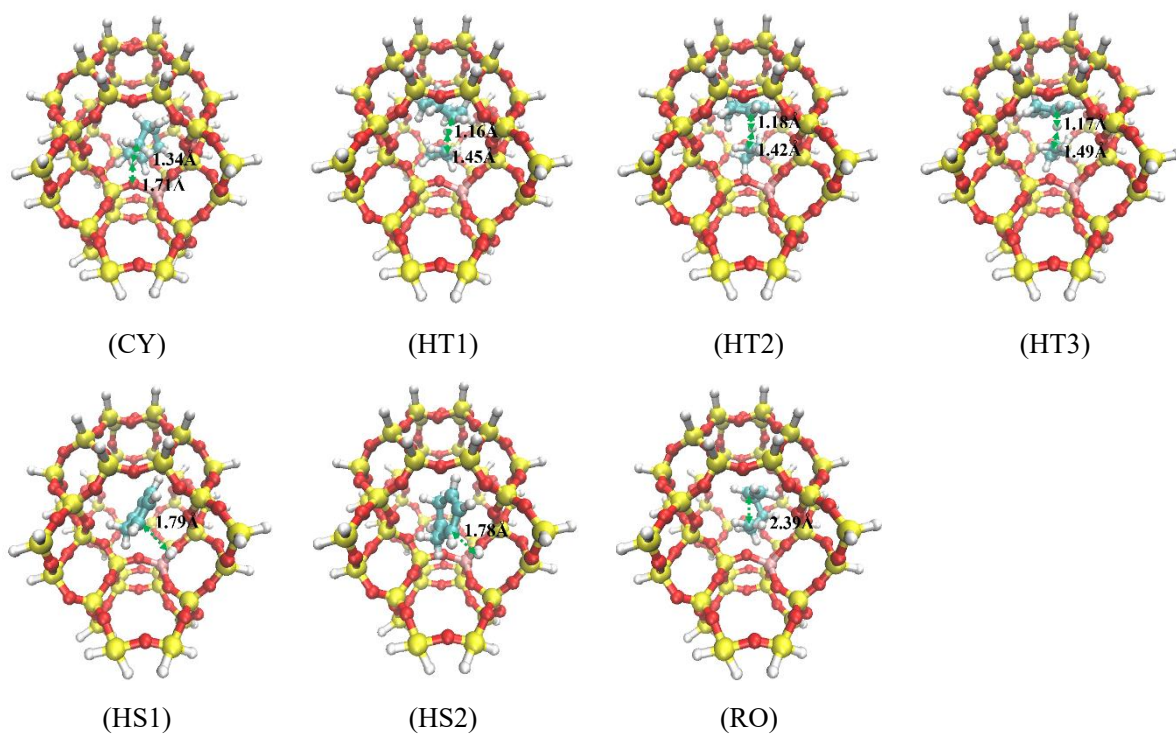
Supplementary Fig. 51. Products distribution. Variation of C2 (ethene+ethane), C3 (propene+propane) and C4 (butene+butane) selectivities with the reaction pressure obtained over GaZrO_x(0.5)/H-SSZ-13(6.0) composite catalyst in direct hydrogenation of CO₂ into propane (typical reaction conditions: H₂/CO₂ = 3:1, GHSV = 2400 mL/(g·h) and 350 °C).



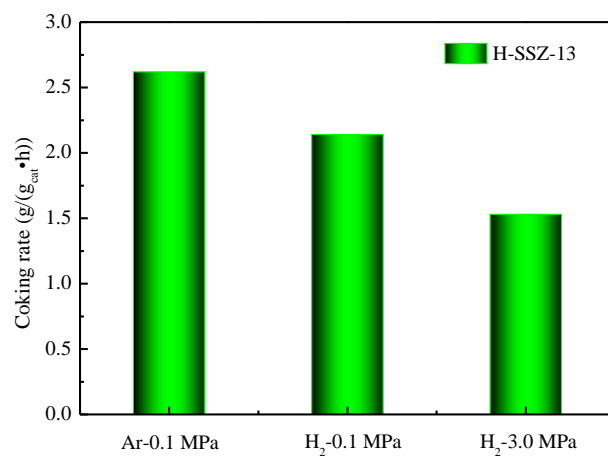
Supplementary Fig. 52. DFT calculation. Reaction network and calculated intrinsic kinetics of various elemental steps for alkene-based cycle, aromatization and aromatics hydrogenolysis reactions over H-SAPO-34. The data represent the free energy barriers (kJ mol^{-1}). M, O, C, H, CY, HT, HS and RO are representative for methylation, oligomerization, cracking, hydrogenation, cyclization, hydride transfer, hydrogenolysis and ring-opening reactions, respectively. ZOH stands for the acidic zeolite.



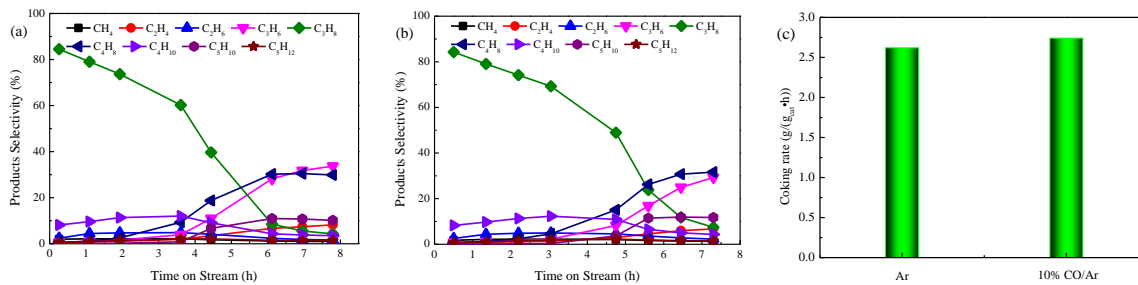
Supplementary Fig. 53. Optimized transition states of various steps in alkene-based cycle over H-SSZ-13.



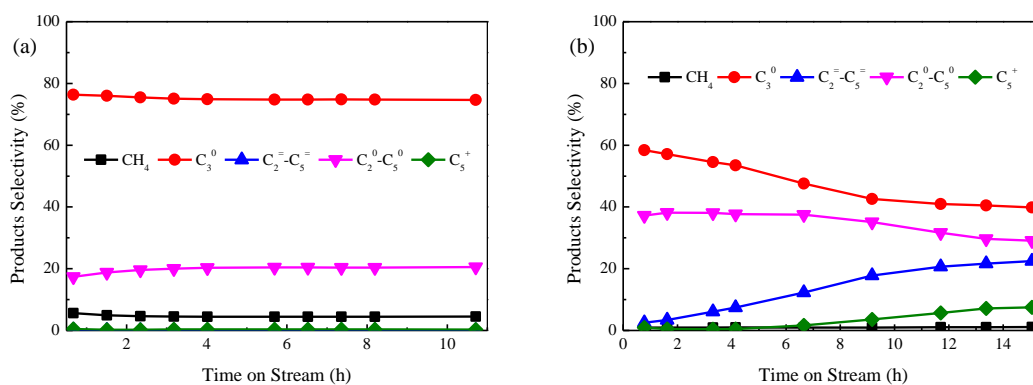
Supplementary Fig. 54. Optimized transition states of various steps in 1-hexene aromatization and aromatic hydrogenolysis on H-SSZ-13.



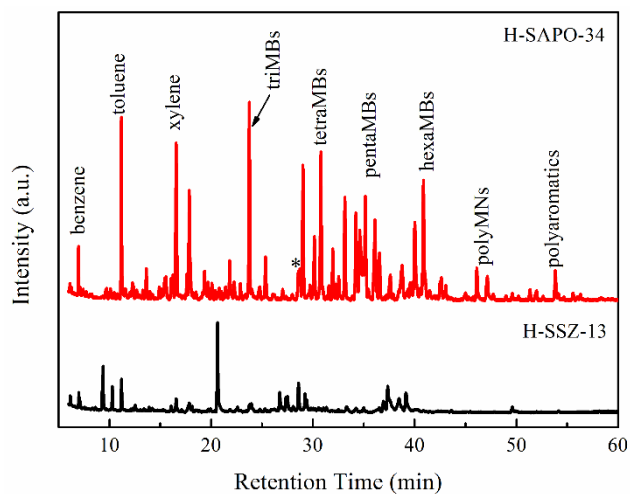
Supplementary Fig. 55. TG analysis. Coking rate obtained from TG analysis at temperature > 200 °C over H-SSZ-13 zeolite after catalyzing methanol conversion (typical reaction conditions: 350 °C and $\text{WHSV}_{\text{methanol}}$ of 0.24 h^{-1}).



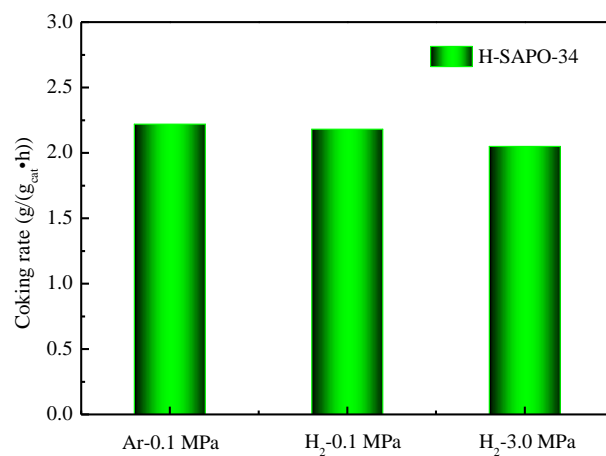
Supplementary Fig. 56. Catalytic performance and TG analysis. The catalytic results for methanol conversion on H-SSZ-13 in Ar (a) and 10%CO/Ar (b) atmospheres, and corresponding coking rate (c) obtained from TG analysis at temperature >200 °C after catalyzing methanol conversion. Typical reaction conditions: 350 °C, 0.1 MPa and $\text{WHSV}_{\text{methanol}}$ of 0.24 h^{-1} .



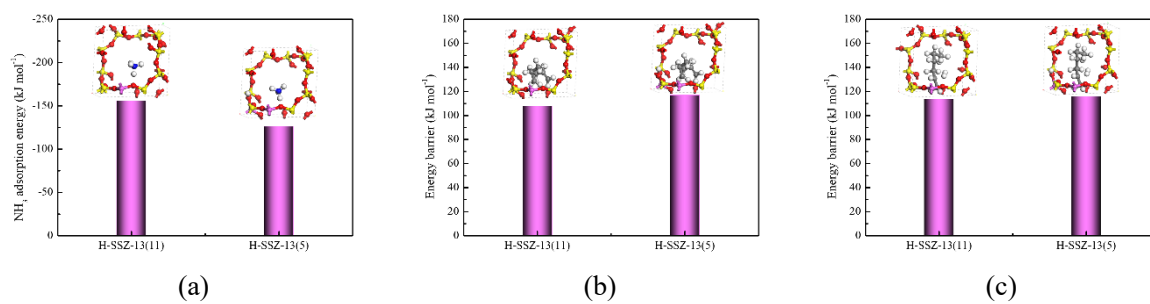
Supplementary Fig. 57. Catalytic performance for 1-hexene conversion. The catalytic results of 1-hexene conversion on H-SSZ-13 (a) and H-SAPO-34 zeolites (b) in H_2 atmosphere (CH_4 , C_3^0 , $C_2^= - C_5^=$, $C_2^0 - C_5^0$ and C_5^+ represent methane, propane, ethene to pentene, ethane to pentane (excluding propane) and other hydrocarbons with carbon number higher than 5, respectively). Typical reaction conditions: 350 °C, 1.5 MPa and $WHSV_{hexene}$ of $0.24\ h^{-1}$.



Supplementary Fig. 58. Retained species on catalysts. GC-MS diagrams of the carbonaceous species confined in the H-SSZ-13(6.0) and H-SAPO-34 after catalyzing 1-hexene conversion at 350 °C, $WHSV_{\text{hexene}}$ of 0.24 h^{-1} and 1.5 MPa (* is the internal standard of hexachloroethane).



Supplementary Fig. 59. TG analysis. Coking rate obtained from TG analyses at temperature > 200 °C over H-SAPO-34 zeolite after catalyzing methanol conversion at different pressure and atmospheres (typical reaction conditions: 350 °C and $WHSV_{\text{methanol}}$ of 0.24 h^{-1}).



Supplementary Fig. 60. DFT calculation. Calculated ammonium adsorption energies (a) and energy barriers of 1-hexene cracking (b) and hydrogenation (c) on H-SSZ-13(11) and H-SSZ-13(5) periodic models.

Supplementary Tables

Supplementary Table 1. Catalytic results of various metal oxide/zeolite bifunctional catalysts for direct hydrogenation of CO₂ into propane.

	Temperature & pressure	CO ₂ con. (%)	CO sel. (%)	CH ₄ (%)	C ₃ ⁰ (%)	C ₃ ⁰ Yield (%)	LPG (%)	LPG Yield (%)	
GaZrO _x (0.5)/H-SSZ-13(6.0)	350 °C, 3.0 MPa	43.4	31.8	4.1	79.5	23.6	89.4	26.5	This work
CuZnAl/Pd-Beta	260 °C, 2.0 MPa	21.2	64.6	3.7	21.1	1.6	81.5	6.1	Ref.4
CuZnZr/Pd-Beta	260 °C, 2.0 MPa	22.0	49.1	3.8	17.8	2.0	74.7	8.3	Ref.4
CuZnZrAl/Pd-Beta	260 °C, 2.0 MPa	25.2	47.3	1.2	12.0	1.6	74.8	9.9	Ref.4
CuZnZr/SAPO-34	350 °C, 2.0 MPa	24.0	58.6	22.8	--	--	75.1	7.5	Ref.5
CuZnZr/MnSAPO-34	350 °C, 2.0 MPa	24.8	78.3	27.1	--	--	68.1	3.7	Ref.5
CuZnZr/ZnSAPO-34	350 °C, 2.0 MPa	25.2	78.0	33.7	--	--	63.7	3.5	Ref.5
CuZnZr/ZrSAPO-34	350 °C, 2.0 MPa	25.7	68.4	9.7	--	--	86.1	7.0	Ref.5
Pd-SiO ₂ /H-ZSM-5	300 °C, 4.0 MPa	5.9	20.1	16.8	--	--	35.6	1.7	Ref.6
PdZn-ZrO ₂ /SAPO-34	350 °C, 5.0 MPa	38.0	25.0	5.0	62.5	17.8	72.5	20.6	Ref.7
In-ZrO _x /SSZ-13	350 °C, 4.0 MPa	24.0	61.0	8.0 ^a	70.0	6.6	90.0	8.5	Ref.8
In-ZrO _x /SAPO-5	300 °C, 3.0 MPa	6.7	55.0	2.0	15.0	1.0	70.0	2.1	Ref.9
In ₂ O ₃ /SAPO-34	400 °C, 2.5 MPa	35.0	85.0	5.0	30.0	1.6	35.0	1.8	Ref.10
Na-Fe ₃ O ₄ /ZSM-5	320 °C, 3.0 MPa	25.6	17.3	6.0	15.0	3.2	40.0	8.4	Ref.11

^a selectivity of methane and ethane.

Supplementary Table 2. Physicochemical properties of ZrO₂, Ga₂O₃ and GaZrO_x(N) oxides with different Ga/Zr molar ratios.^a

Catalysts	Phase	S _{BET} (m ² g ⁻¹)	V _{micro} (cm ³ g ⁻¹)	<i>d</i> _{size} (nm)	<i>D</i> _{size} (nm)	Cell volume (Å ³)
ZrO ₂	tetragonal	13.0	0.001	5.4	6.4(10.53)	67.2374
GaZrO _x (0.1)	tetragonal	46.0	0.003	4.6	5.8 (8.50)	66.9070
GaZrO _x (0.25)	tetragonal	73.0	0.004	4.3	5.4	66.4298
GaZrO _x (0.5)	tetragonal	113.1	0.005	3.6	4.4 (5.76)	65.9804
GaZrO _x (1.0)	tetragonal	159.1	0.007	3.6	2.9	65.7013
GaZrO _x (4.0)	amorphous	161.8	0.008	4.3	--	--
Ga ₂ O ₃	amorphous	30.5	0.001	4.5	--	--

^a The crystalline phases and cell volume of various samples were identified and calculated by the Rietveld refinement of XRD patterns. The surface area (S_{BET}), pore volume (V_{micro}), and average pore size (*d*_{size}) were obtained on the basis of nitrogen sorption isotherms by the BET, t-plot, and BJH methods, respectively. The average particle sizes of NPs (*D*_{size}) were estimated by the XRD and TEM (in parentheses) techniques.

Supplementary Table 3. Chemical compositions, texture properties and acidity of various H-SSZ-13 and H-SAPO-34 zeolites.

Zeolites	Si/Al ratio ^a	Surface area		Pore volume		Acid content		
		(m ² g ⁻¹) ^b		(cm ³ g ⁻¹) ^b		(mmol g ⁻¹) ^c		
		Total	Micro	Total	Micro	Weak	Medium	Strong
H-SSZ-13(3.3)	3.4	270.3	247.7	0.16	0.13	0.408 (175°C)	0.672 (221°C)	0.194 (432°C)
H-SSZ-13(6.0)	6.5	527.5	471.7	0.35	0.24	0.723 (181°C)	0.179 (246°C)	0.559 (463°C)
H-SSZ-13(9.6)	10.6	598.9	513.0	0.45	0.26	0.583 (176°C)	0.118 (360°C)	0.659 (472°C)
H-SSZ-13(15.6)	16.2	616.4	547.6	0.38	0.27	0.388 (171°C)	0.111 (373°C)	0.420 (456°C)
H-SSZ-13(22.0)	21.8	601.4	540.4	0.34	0.27	0.258 (167°C)	0.074 (346°C)	0.369 (447°C)
H-SAPO-34	0.14	496.8	433.8	0.29	0.22	0.274 (170°C)	0.716 (349°C)	0.085 (396°C)

^a The Si/Al ratios of H-SSZ-13 samples were measured by ICP-AES. ^b The surface area and pore volume were determined on the basis of nitrogen sorption isotherms by using the BET method and t-plot method respectively. ^c The contents of weak, moderately strong (M-strong) and strong acid sites were determined from NH₃-TPD profiles by estimating the quantities of ammonia desorbed at 120–200 °C, 200–400 °C and 400–600 °C, respectively. The data in the parentheses represent the desorption peak temperature (°C) of NH₃ interacted with weak, moderately strong and strong acid sites.

Supplementary Table 4. Calculated energy barriers for 1-hexene cracking and hydrogenation with cluster and periodic H-SSZ-13 models.

	Cluster model	Periodic model
1-hexene cracking	98 kJ mol ⁻¹	108 kJ mol ⁻¹
1-hexene hydrogenation	134 kJ mol ⁻¹	125 kJ mol ⁻¹

Supplementary Methods

Preparation of other zeolites. SAPO-34 (CHA), ZSM-11 (MEL) and ZSM-35 (FER) zeolites were prepared by the hydrothermal synthesis method. For SAPO-34 zeolite, the silica sol (JN-40), phosphoric acid (H_3PO_4), pseudo-boehmite (Al_2O_3), tetraethyl ammonium hydroxide (TEAOH) and deionized water were mixed and stirred at room temperature for 2 h in terms of a composition of 2.0TEAOH: 0.3SiO₂: 1.0Al₂O₃: 1.0P₂O₅: 70H₂O. ZSM-11 zeolite was prepared by using the silica sol (JN-40), deionized water, tetrabutylammonium hydroxide (TBAOH), sodium aluminate (NaAlO_2) and sodium hydroxide (NaOH) with the ratio of mixture of 12TBAOH: 5.0Al₂O₃: 120SiO₂: 1420H₂O: 8.6Na₂O. The obtained mixture was then stirred at room temperature for 2 h. ZSM-35 zeolite was synthesis with the silica sol (JN-40), pyrrolidine (PYR), sodium hydroxide (NaOH), sodium aluminate (NaAlO_2) and deionized water. The mixture was stirred at room temperature for 4 h. The obtained gel had a composition of 1.85Na₂O: 1.0Al₂O₃: 20SiO₂: 19.7PYR: 592H₂O. The resultant gel was then transferred into a Teflon-lined stainless-steel autoclave and crystallized at 200 °C for 20 h for SAPO-34, 170 °C for 20 h and 48 h for ZSM-11 and ZSM-35, respectively.

Various H-type zeolite samples of H-SSZ-13, H-ZSM-11 and H-ZSM-35 were obtained by repeatedly ion-exchanging calcined Na-type samples with 1 M NH_4NO_3 aqueous solution at 80 °C for three times, drying at 100 °C for 12 h, and calcining at 560 °C for 5 h. For the preparation of H-SAPO-34, the as-synthesized sample was directly calcined at 550 °C for 10 h in air.

Catalysts characterizations. For the in situ DRIFTS, 50 mg sample was placed in the cell and pretreated at 400 °C for 2 h in a H₂ flow (30 mL/min). Then, it was purged with Ar (30 mL/min) for 0.5 h. Afterwards, it was cooled to the reaction temperature of 300 °C and the background spectrum was collected. For the CO₂ hydrogenation, the sample was exposed to a CO₂ and H₂(D₂) mixture flow (CO₂/H₂(D₂) = 1/3, flow rate = 40 mL/min) at reaction temperature. The spectra in the range of 4000–1000 cm⁻¹ were collected every 5 min up to 60 min at a resolution of 4 cm⁻¹ by accumulating 64 scans.

Model system for DFT calculations. The tetragonal ZrO₂(101) ($a = b = 3.6420 \text{ \AA}$, $c = 5.2750 \text{ \AA}$) was modeled by a nine-atomic-layer slabs with a (2 × 3) super unit cell.¹² The top three layers of the model system were relaxed, whereas the other layers in bottom were fixed at their optimized bulk positions. A vacuum spacing of 15 Å was assumed to exist between the periodic slab models along the normal direction (z) for avoiding spurious interactions. The Monkhorst Pack mesh k -points of (2 × 2 × 1) were applied for the calculations by allowing convergence to 1×10^{-4} eV for the total electronic energy and below 0.05 eV/Å for the remaining total force. To construct the model of gallium-zirconium oxide, corresponding numbers of Zr atoms on the surface of ZrO₂ were substituted by Ga atoms to simulate the GaZrO_x(0.5) and GaZrO_x(4.0) oxides, as reported on ZnZrO_x and InZrO_x.^{13,14} This is because CO₂ hydrogenation to methanol mainly occurs on the surface of metal oxide. Certainly, large amounts of Ga species are also incorporated in the bulk of ZrO₂, as Ga species are assumed to homogeneously distribute in the sample. With respect to the gas-phase species of CO₂, H₂ and CO, Γ -point calculations were carried using a (15 × 15 × 15) Å³ box. Transition state structures were obtained by the climbing image nudged elastic band

method (CI-NEB).¹⁵ For each optimized stationary point, vibrational analysis was performed at the same level of theory to determine its character (minimum or saddle point). Atomic charges were calculated by using the grid-based Bader analysis algorithm developed by Henkelman and co-workers.^{16,17}

H-SSZ-13 and H-SAPO-34 zeolite were simulated by the 46 T cluster model that covers the supercages ($6.7 \times 10 \text{ \AA}$) and 8-membered-ring windows ($3.8 \times 3.8 \text{ \AA}$). The 7T active region and the reacting molecules were treated as the high layer, whereas the rest of the structure was considered as the low layer. Transition states (TS) were guessed by the OPT=TS method and confirmed by verifying that each transition state was connected to the corresponding reactants and products by the quasi-internal reaction coordinate (quasi-IRC) approach. The transition state is a first-order saddle point of potential energy surface with only a single imaginary frequency. The obtained reactants and products were situated in the energy minima points of potential energy surface with only real frequencies. This cluster model has been substantiated to give reliable results for the reaction kinetics of various elementary steps in methanol conversion.^{18,19} Indeed, similar energy barriers were obtained with the cluster model and the periodic CHA model for 1-hexene cracking and hydrogenation reactions (Supplementary Table 4), confirming the current cluster model reliability.

To theoretically evaluate the Si/Al ratio effect of zeolite on the reaction kinetics, two CHA periodic models with one and two framework Al atoms in one unit cell, which are corresponding to the Si/Al ratio of 11 (H-SSZ-13(11)) and 5 (H-SSZ-13(5)), respectively, were constructed. The calculation results indicate that the energy barrier for 1-hexene

cracking and hydrogenation reactions on H-SSZ-13(11) is highly comparable to that on H-SSZ-13(5), due to their similar acid site strength, as confirmed by the calculated ammonia adsorption energy ($\Delta E_{\text{NH}_3\text{-ads}}$) (Supplementary Fig. 60). This is consistent with the catalytic results of H-SSZ-13(6.0) and H-SSZ-13(9.6) with similar strong acid site content and strength; both the samples show similar CO₂ conversion and product selectivity in CO₂ hydrogenation to propane (Fig. 1, Supplementary Fig. 4 and Supplementary Table 3).

Calculation methods for conversion and product selectivity. For the CO₂ hydrogenation reactions, the CO₂ conversion was calculated by the equation (1), and the selectivity to hydrocarbons (including alkenes and alkanes, C_nH_m) and oxygenates (including methanol (CH₃OH) and dimethyl ether (DME)) were calculated by the equations (3) and (4), respectively, without considering CO. The CO emission was separately evaluated by the equation (2). The carbon molar balances were around 95%.

$$\text{CO}_2 \text{ conversion} = \frac{\text{CO}_{2\text{in}} - \text{CO}_{2\text{out}}}{\text{CO}_{2\text{in}}} \times 100\% \quad (1)$$

$$\text{CO selectivity} = \frac{\text{CO}_{\text{out}}}{\text{CO}_{2\text{in}} - \text{CO}_{2\text{out}}} \times 100\% \quad (2)$$

where CO_{2in} and CO_{2out} are the inlet and outlet amounts (moles) of CO₂ respectively; CO_{out} is the outlet amount (mole) of CO.

$$\text{C}_n\text{H}_m \text{ selectivity} = n_{\text{C}_n\text{H}_m} / \sum(\text{C}_n\text{H}_m + \text{oxygenates}) \times 100\%; \quad (3)$$

$$\text{Oxygenates selectivity} = n_{\text{oxygenates}} / \sum(\text{C}_n\text{H}_m + \text{oxygenates}) \times 100\%; \quad (4)$$

where $n_{\text{C}_n\text{H}_m}$ is the amount (carbon moles) of individual hydrocarbon product at the outlet and $\sum(\text{C}_n\text{H}_m + \text{oxygenates})$ is the total carbon mole of products, including all

hydrocarbons and oxygenates. The catalytic results obtained at reaction time of ~28 h were generally used for comparison.

The methanol conversion (x_{methanol}) or 1-hexene conversion ($x_{\text{1-hexene}}$) and the selectivity to product i (s_i) were calculated by the following equations:

$$x_{\text{methanol}} = (n_{\text{methanol,in}} - n_{\text{methanol,out}}) / n_{\text{methanol,in}} \times 100\% \quad (5)$$

$$x_{\text{1-hexene}} = (n_{\text{1-hexene,in}} - n_{\text{1-hexene,out}}) / n_{\text{1-hexene,in}} \times 100\% \quad (6)$$

$$s_i = n_i \cdot k_i / \sum n_i \cdot k_i \times 100\% \quad (7)$$

where n_i is the molar quantity of product i in the effluents and k_i is the number of carbon atoms in its molecule.

Supplementary References

- (1) Liang, F. L., Yu, Y., Zhou, W., Xu, X. Y. & Zhu, Z. H. Highly defective CeO₂ as a promoter for efficient and stable water oxidation. *J. Mater. Chem. A* **3**, 634–640 (2015).
- (2) Wang, S., Wang, P. F., Shi, D. Z., He, S. P., Zhang, L., Yan, W. J., Qin, Z. F., Li, J. F., Dong, M., Wang, J. G. Olsbye, U. & Fan, W. B. Direct conversion of syngas into light olefins with low CO₂ emission. *ACS Catal.* **10**, 2046–2059 (2020).
- (3) Wang, S., Zhang, L., Zhang, W. Y., Wang, P. F., Qin, Z. F., Yan, W. J., Dong, M., Li, J. F., Wang, J. G., He, L., Olsbye, U. & Fan, W. B. Selective conversion of CO₂ into propene and butene. *Chem* **6**, 3344–3363 (2020).
- (4) Li, C. M., Yuan, X. D. & Fujimoto, K. Direct synthesis of LPG from carbon dioxide over hybrid catalysts comprising modified methanol synthesis catalyst and -type zeolite. *Appl. Catal. A: Gen.* **475**, 155–160 (2014).
- (5) Tong, M. L., Hondo, E., Chizema, L. G., Du, C., Ma, Q. X., Mo, S. T., Lu, C. X., Lu, P. & Tsubaki, N. Hydrogenation of CO₂ to LPG over CuZnZr/MeSAPO-34 catalysts. *New J. Chem.* **44**, 9328–9336 (2020).
- (6) Li, H. J., Zhang, P. P., Guo, L. S., He, Y. L., Zeng, Y., Thongkam, M., Natakaranakul, J., Kojima, T., Reubroycharoen, P., Vitidsant, T., Yang, G. H. & Tsubaki, N. Well-defined core-shell-structured capsule catalyst for direct conversion of CO₂ into liquefied petroleum gas. *ChemSusChem.* **13**, 2060–2065 (2020).
- (7) Ramirez, A., Ticali, P., Salusso, D., Cordero-Lanzac, T., Ould-Chikh, S., Ahoba-Sam, C., Bugaev, A. L., Borfecchia, E., Morandi, S., Signorile, M., Bordiga, S., Gascon, J. & Olsbye, U. Multifunctional catalyst combination for the direct conversion of CO₂ to propane. *JACS Au* **1**, 1719–1732 (2021).
- (8) Liu, Z. P., Ni, Y. M., Sun, T. T., Zhu, W. L. & Liu, Z. M. Conversion of CO₂ and H₂ into propane over InZrO_x and SSZ-13 composite catalyst. *J. Energy Chem.* **54**, 111–117 (2021).
- (9) Wang, J. Y., Zhang, A. F., Jiang, X., Song, C. S. & Guo, X. W. Highly selective conversion of CO₂ to lower hydrocarbons (C₂-C₄) over bifunctional catalysts composed of In₂O₃-ZrO₂ and zeolite. *J. CO₂ Util.* **27**, 81–88 (2018).
- (10) Numpilai, T., Wattanakit, C., Chareonpanich M. & Limtrakul, J. Optimization of

- synthesis condition for CO₂ hydrogenation to light olefins over In₂O₃ admixed with SAPO-34. *Energ. Convers. Manage.* **180**, 511–523 (2019).
- (11) Wei, J., Yao, R. W., Ge, Q. J., Wen, Z. Y., Ji, X. W., Fang, C. Y., Zhang, J. X., Xu, H. Y. & Sun, J. Catalytic hydrogenation of CO₂ to isoparaffins over Fe-based multifunctional catalysts. *ACS Catal.* **8**, 9958–9967 (2018).
- (12) Zhang, M. H., Zhuang, J. Y. & Yu, Y. Z. A DFT study on ZrO₂ surface in the process of ethanol to 1,3-butadiene: A comprehensive mechanism elucidation. *Appl. Surf. Sci.* **458**, 1026–1034 (2018).
- (13) Gao, P., Dang, S. S., Li, S. G., Bu, X. N., Liu, Z. Y., Qiu, M. H., Yang, C. G., Wang, H., Zhong, L. S., Han, Y., Liu, Q., Wei, W. & Sun, Y. H. Direct production of lower olefins from CO₂ conversion via bifunctional catalysis. *ACS Catal.* **8**, 571–578 (2018)
- (14) Wang, J. J., Li, G. N., Li, Z. L., Tang, C. Z., Feng, Z. C., An, H. Y., Liu, H. L., Liu, T. F. & Li, C. A highly selective and stable ZnO-ZrO₂ solid solution catalyst for CO₂ hydrogenation to methanol. *Sci. Adv.* **3**, e1701290 (2017).
- (15) Henkelman, G. & Jónsson, H. Improved tangent estimate in the nudged elastic band method for finding minimum energy paths and saddle points. *J. Chem. Phys.* **113**, 9978–9985 (2000).
- (16) Henkelman, G., Arnaldsson, A. & Jonsson, H. A fast and robust algorithm for Bader decomposition of charge density, *Comput. Mater. Sci.* **36**, 354–360 (2006).
- (17) Sanville, E., Kenny, S. D. Smith, R. & Henkelman, G. Improved grid-based algorithm for Bader charge allocation, *J. Comput. Chem.* **28**, 899–908 (2007).
- (18) Hemelsoet, K., Nollet, A., Van Speybroeck, V. & Waroquier, M. Theoretical Simulations Elucidate the Role of Naphthalenic Species during Methanol Conversion within H-SAPO-34. *Chem. Eur. J.* **17**, 9083–9093 (2011).

- (19) Zhang, W. N., Zhang, M. Z., Xu, S. T., Gao, S. S., Wei, Y. X. & Liu, Z. M. Methylcyclopentenyl cations linking initial stage and highly efficient stage in methanol-to-hydrocarbon process. *ACS Catal.* **10**, 4510–4516 (2020).